arXiv:1503.08555v1 [astro-ph.GA] 30 Mar 2015

INFRARED AND X-RAY EVIDENCE OF AN AGN IN THE NGC 3256 SOUTHERN NUCLEUS

Youichi Ohyama[1], Yuichi Terashima[2], and Kazushi Sakamoto[1]

[1]Academia Sinica, Institute of Astronomy and Astrophysics, No.1, Sec. 4, Roosevelt Rd, Taipei 10617, Taiwan, R.O.C. and
[2]Department of Physics, Ehime University, Matsuyama, Ehime 790-8577, Japan

Draft version March 31, 2015

ABSTRACT

We investigate signs of Active Galactic Nucleus (AGN) in the luminous infrared galaxy NGC 3256 at both infrared and X-ray wavelengths. NGC 3256 has double, the Northern and Southern, nuclei (hereafter, N and S nuclei, respectively). We show that the *Spitzer* IRAC colors extracted at the S nucleus are AGN-like, and the *Spitzer* IRS spectrum is bluer at < 6 μm than at the N nucleus. We built for the S nucleus an AGN-starburst composite model with a heavily absorbed AGN to successfully reproduce not only the IRAC and IRS specrophotometries at $\simeq 3''$ but also the very deep silicate 9.7 μm absorption observed at $0{.}''36$ scale by Díaz-Santos et al. We found a 2.2 μm compact source at the S nucleus in a *HST* NICMOS image and identified its unresolved core (at $0{.}''26$ resolution) with the compact core in previous mid-infrared observations at comparable resolution. The flux of the 2.2 μm core is consistent with our AGN spectral energy distribution model. We also analyzed a deeper than ever *Chandra* X-ray spectrum of the unresolved (at $0{.}''5$ resolution) source at the S nucleus. We found that a dual-component power-law model (for primary and scattered ones) fits an apparently very hard spectrum with a moderately large absorption on the primary component. Together with a limit on equivalent width of a fluorescent Fe-K emission line at 6.4 keV, the X-ray spectrum is consistent with a typical Compton-thin Seyfert 2. We therefore suggest that the S nucleus hosts a heavily absorbed low-luminosity AGN.

Subject headings: infrared: galaxies — X-rays: galaxies — galaxies: active — galaxies: individual (NGC 3256) — galaxies: nuclei

1. INTRODUCTION

Occurrence of Active Galactic Nuclei (AGNs) in Luminous Infrared Galaxies (LIRGs) has been extensively discussed since there are many lines of evidence for direct and causal relationship between them. LIRGs predominantly emit at far infrared (FIR), and the infrared (IR) luminosities at 8–1000 μm, L_{IR}, amount to $11 < \log L_{IR}$ (L$_\odot$) < 12 by definition (Sanders & Mirabel 1996). Although bulk of the energy in LIRGs is due to intense star formation activity (Sanders & Mirabel 1996), AGNs are often found among LIRGs. Also, a significant fraction of LIRGs are tidally interacting objects. The fraction of AGN-dominated sources is known to be higher in LIRGs with larger IR luminosity (e.g., Veilleux et al. 1995; Kim et al. 1995; Nardini et al. 2008, 2010; Petric et al. 2011; Iwasawa et al. 2011; Alonso-Herrero et al. 2012) and in later interaction stages (Petric et al. 2011; Iwasawa et al. 2011).

Both mid-infrared (MIR) and X-ray studies are very effective to reveal nuclear activities in LIRGs. Although LIRGs, in particular their nuclei, are often heavily absorbed at optical and near-infrared (NIR) wavelengths, both MIR and hard X-ray photons can penetrate through such interstellar medium. We can study AGN indications at MIR because AGNs typically show characteristic power-law-like spectral energy distribution (SED), which often shows an excess at MIR over the SED from warm and cold dusts (e.g., Granato et al. 1997; Alonso-Herrero et al. 2001; Nenkova et al. 2002; Armus et al. 2007; Donley et al. 2012). Various kinds of AGN diagnostics have been developed at MIR, and empirical assessments of relative AGN contribution to the entire

system have been made (Genzel et al. 1998; Sturm et al. 2002; Armus et al. 2007; Spoon et al. 2007; Desai et al. 2007; Petric et al. 2011; Stierwalt et al. 2013). We can also study typical AGNs at X-ray because AGNs show luminous and characteristic power-law spectra, the hard part of which suffers from less absorption by circum-AGN material. Therefore, X-ray has been heavily utilized to study AGN in LIRGs (e.g., Iwasawa et al. 2011).

NGC 3256 is the most luminous LIRG in the local universe ($z < 0.01$). At a distance of 35 Mpc (for consistency with Sakamoto et al. 2014, which adopted Sanders et al. 2003[1]), its IR luminosity (L_{IR}) is as large as 3.6×10^{11} L$_\odot$ (Sanders et al. 2003), or total IR luminosity at 3–1100 μm (TIR) is $(2.7–3.3)\times10^{11}$ L$_\odot$(Engelbracht et al. 2008 converted for our assumed distance). It is also among the most luminous X-ray sources without a confirmed AGN in the local universe (Moran et al. 1999; Lira et al. 2002; Pereira-Santaella et al. 2011). It is a major merging system showing tidally distorted morphology at galaxy scale with tidal tails, disturbed outer spiral arms, and prominent dust lanes with complex morphology (e.g., Graham et al. 1984; Kotilainen et al. 1996; Zepf et al. 1999; Lípari et al. 2000; Alonso-Herrero et al. 2002; English et al. 2003; Alonso-Herrero et al. 2006a,b; Sakamoto et al. 2014). Its double nuclei, often referred to as Northern and Southern nuclei (hereafter, N and S nuclei, respectively) are separated by only 5$''$ (850 pc). They are clearly visible at both radio and MIR (e.g., Nor-

---

[1] Sanders et al. (2003) adopted distance with cz using the cosmic attractor model outlined in Appendix A of Mould et al. (2000), using $H_0 = 75$ km s^{-1} Mpc^{-1} and adopting a flat cosmology in which $\Omega_M = 0.3$ and $\Omega_\lambda = 0.7$.

ris & Forbes 1995; Kotilainen et al. 1996; Neff et al. 2003; Alonso-Herrero et al. 2006b; Lira et al. 2008; Sakamoto et al. 2014), but the S nucleus is hidden in dust at the optical. The merger is likely in the late stage just before coalescence of the nuclei (Armus et al. 2009; Stierwalt et al. 2013).

The N nucleus is a core of a starburst galaxy. Its optical spectrum shows H II region-like features. Extended outflowing ionized gas with shocks is also detected and attributed to a superwind powered by the starburst (Moran et al. 1999; Lípari et al. 2000; Rich et al. 2012; Bellocchi et al. 2013). Stellar population examined in K band indicates young starburst population (Doyon et al. 1994). Prominent Polycyclic Aromatic Hydrocarbon (PAH) features as well as low-ionization fine structure lines have been detected at MIR (Siebenmorgen et al. 2004; Martín-Hernández et al. 2006; Lira et al. 2008; Pereira-Santaella et al. 2010; Díaz-Santos et al. 2010a), also indicating star formation activity. The nucleus is spatially resolved with HST at 1.6 μm at $0\rlap{.}''14$ full-width half maximum (FWHM) resolution (Alonso-Herrero et al. 2002), the 8.1 m Gemini Telescope at 8.74 μm at its diffraction-limit ($0\rlap{.}''30$ FWHM) resolution (Alonso-Herrero et al. 2006b), and $Chandra$ at X-ray at $0\rlap{.}''5$ FWHM resolution (Lira et al. 2002).

Presence of an AGN at the optically obscured S nucleus has been suspected for a long time (e.g., Kotilainen et al. 1996), but there is still no firm evidence for it. Dust lanes cover the S nucleus and make it invisible at optical and NIR wavelengths below K band. A compact (unresolved at $0\rlap{.}''5$ FWHM) and moderately absorbed (neutral Hydrogen column density $N_{\rm H} \simeq 5 \times 10^{22}$ cm^{-2}) X-ray source was detected with $Chandra$ at this nucleus (Lira et al. 2002). Although it looks much fainter (by at least two orders of magnitude) than expected for a classical Seyfert nucleus given its MIR luminosity, it is brighter than expected for typical starburst galaxies (Lira et al. 2002; see also Awaki et al. 1991; Turner et al. 1997; Guainazzi et al. 2005; Fukazawa et al. 2011). Analysis of the MIR SED extracted within a kpc-scale aperture (including both nuclei and the host galaxy component) indicated that AGN contribution to the total MIR luminosity is $< 5\%$ (Alonso-Herrero et al. 2012). Sakamoto et al. (2014) recently discovered a bipolar collimated jet-like molecular-gas outflow from the S nucleus, and argued that it is likely driven by an AGN.

Due to its proximity, NGC 3256 is among the best targets to examine the characteristics and roles of AGN, if any, within a LIRG system. For this purpose, it is essential to verify the presence of an AGN in the S nucleus using spatially resolved and/or sensitive MIR and X-ray observations (e.g., Lira et al. 2002; Díaz-Santos et al. 2010b, 2011; Pereira-Santaella et al. 2010). Recent spatially-resolved MIR spectroscopies revealed some interesting differences between the two nuclei. By using the slit-scanning spectroscopy data taken with the $Spitzer$ IRS (Houck et al. 2004), Pereira-Santaella et al. (2010) noted that the S nucleus shows deeper silicate absorption at 9.7 μm, stronger H$_2$ lines, and a slightly smaller equivalent width (EW) of PAH 6.2 μm than those at the N nucleus. More dramatic differences are found in ground-based spectra obtained with higher-spatial resolution. The silicate absorption is much deeper and the

PAH features are undetectably weaker at $0\rlap{.}''36$ (61 pc) scale at the S nucleus than in the IRS spectrum (Díaz-Santos et al. 2010a). At X-ray, Lira et al. (2002) reported that the point-like source at the S nucleus is more heavily absorbed than other point sources and the diffuse component within the galaxy. In this work we utilize archival and published data of $Spitzer$, HST, and $Chandra$ to analyze the nuclear spectrophotometry more comprehensively than ever to explore an AGN in the S nucleus.

2. INFRARED DATA

2.1. $Spitzer$ IRAC

We examined $Spitzer$ IRAC (Fazio et al. 2004) archival images of NGC 3256 at its four channels for morphological and photometric studies. Although Lira et al. (2008) (see also Lira et al. 2002) published the IRAC images and provided nuclear photometries, they did not use the 8.0 μm channel image in their analysis because it is slightly saturated at around the N nucleus. The 8.0 μm information is helpful in conjunction with information of the 3.6, 4.5, and 5.8 μm channels to create IRAC color-color diagrams for AGN diagnostics (e.g., Lacy et al. 2004; Sajina et al. 2005; Stern et al. 2005; Donley et al. 2012). Fortunately, the images were taken under the HDR (High Dynamic Range) mode in which both short- and long-exposure frames are taken within an Astronomical Observation Request (AOR). The short-exposure frame is not saturated at the N nucleus. We retrieved the Post Basic-Calibrated Data (Post BCD or PBCD) of standard mapping observations (AOR: 3896832; PI: G. Fazio) from the $Spitzer$ Heritage Archive. This is the same data set of Lira et al. (2002, 2008). For the 8.0 μm channel, since short-exposure frames are not recommended for science use in general (IRAC data handling book), we confirmed flux calibration consistency between the long- and short-exposure frames using photometry of field stars. Then the saturated pixels at around the N nucleus in the long-exposure frame were substituted with corresponding pixels in the short-exposure frame image. For the 4.5 μm channel, additional simple sky subtraction was made to correct for its tilted background. As shown by Lira et al. (2008) for the 3.6, 4.5, and 5.8 μm channels, the two compact nuclei are clearly separated in all four channels (Figure 1).

Aperture photometry was made on each nucleus with our IDL program (Table 1). We used an aperture of $2\rlap{.}''8$ diameter for the photometry, and applied aperture correction following Surace et al. (2004). Flux contribution from the host galaxy is estimated within a concentric annulus whose inner and outer radii are $2\rlap{.}''0$ and $2\rlap{.}''6$, respectively. The size of the annulus was set as small as possible to estimate the flux level near the nucleus by minimizing the effect of host galaxy structure. Standard deviation within the annulus is quadratically added to the statistical error of the flux measurement of the nuclei. Although our fluxes are systematically slightly fainter than those of Lira et al. (2008), the two are consistent because Lira et al. (2008) performed simple aperture photometry with slightly larger apertures than ours ($3\rlap{.}''6$, $3\rlap{.}''6$, and $4\rlap{.}''0$ diameter apertures for the 3.6 μm, 4.5 μm, and 5.8 μm images, respectively). We note that N nucleus has only about 7%, 7%, 6%, and 7%, and the S nucleus has about 4%, 9%, 4%, and 2% in 3.6 μm,

4.5 μm, 5.8 μm, and 8.0 μm channels, respectively, of the flux integrated over the entire galaxy reported by Engelbracht et al. (2008). Flux ratio maps were also made for 4.5 μm/3.6 μm, 5.8 μm/4.5 μm, and 8.0 μm/5.8 μm (Figure 2). The point spread function (PSF) size matching was made for these ratio maps using a bright field star as a reference. The measured PSF FWHM is about 2.9 pixel or 1″.7.

2.2. *Spitzer IRS*

We processed our own IRS spectra so that the spectrophotometry was done in a way consistent with the corresponding IRAC photometry for each nucleus, although similar spectra had been already published (Brandl et al. 2006; Bernard-Salas et al. 2009; Pereira-Santaella et al. 2010; Díaz-Santos et al. 2010a; Alonso-Herrero et al. 2012). We used the same IRS mapping data set of Pereira-Santaella et al. (2010) and Alonso-Herrero et al. (2012), and followed almost the same processing methods as adopted in the earlier studies. The BCD data (AOR: 17659904; PI: G. Rieke) of the Short-Low (SL) module were retrieved from the *Spitzer* Heritage Archive. Similar mapping data with other modules (Long-Low (LL), Long-High (LH), and Short-High (SH)) were not used since spatial resolution was worse for the longer wavelength data. They are not suitable for our analysis in which separating the two nuclei is essential. The standard CUBISM data processing (Smith et al. 2007a; Pereira-Santaella et al. 2010) was made, including background subtraction, hot/rogue pixel identification and subtraction, and cube creation.

Aperture photometry was made with our IDL program to extract spectra for each nucleus on the data cubes created with CUBISM (Figure 3). We fixed an aperture size of 3″.6 diameter over 5.2–14.5 μm and applied the aperture correction. Flux contribution from the host galaxy is estimated within a concentric annulus whose inner and outer radii are 2″.0 and 2″.6, respectively. The size of the annulus was set as small as possible to estimate flux level near the nucleus by minimizing the effect of host galaxy structure. However, since the IRS spatial resolution ($\simeq 4''$ FWHM) is larger than that of IRAC and is comparable to the distance to another nucleus ($\simeq 5''$), we carefully applied masks to hide another nuclear component in the annulus. Standard deviation within the annulus is quadratically added to the statistical error of the flux measurement of the nuclei. The aperture correction factor was measured with a mapping observation of a standard star, HR 7341. The standard star data (AOR 19324160) taken in the same observing campaign of the NGC 3256 observation were retrieved from the *Spitzer* Heritage Archive, and they were reduced by CUBISM with exactly the same parameters. We then measured the star with the same photometry program and aperture settings, and found the aperture correction factor by comparing the measured spectrum with the standard-star flux information from the IRS Instrument Handbook.

As in the case of the IRAC photometry, those nuclear spectrophotometries are about 12–20% of that over the entire galaxy (13″.4 × 13″.4; Alonso-Herrero et al. 2012), although the overall spectral shapes look similar, i.e., all show prominent PAH 6.2, 7.7, 8.6, 11.3 μm features and fine structure lines such as [Ne II]. We confirmed

characteristics reported earlier by Pereira-Santaella et al. (2010), namely brighter H_2 fluxes, deeper silicate absorption at 9.7 μm, and smaller EW of PAH 6.2 μm at the S nucleus (see §3.2 below for our silicate absorption depth measurements).

2.2.1. *Flux Matching between the IRAC and IRS Spectrophotometries*

The IRS nuclear photometries are about two times larger than the IRAC 5.8 μm and 8.0 μm nuclear photometries at both nuclei (Figure 3), and we interpret this as a result of more contamination from the host component due to larger PSF of IRS. Therefore, in order to combine the IRS and IRAC spectrophotometries in a consistent way for our subsequent analyses, we adjusted the IRAC nuclear photometries for the IRS resolution in the following way. For the N nucleus, we simply scaled the observed nuclear IRAC fluxes by a factor measured at both 5.8 μm and 8.0 μm channels by comparing with synthetic IRAC fluxes from the IRS spectrum. We utilized a standard photometry tool (spitzer_synthphot.pro) from *Spitzer* Data Analysis Cookbook. Since the IRS SL module cannot fully cover the IRAC 5.8 μm bandpass between 4.9 and 5.2 μm, we extrapolated the spectra shortward a little with a help of scaled SWIRE NGC 6090 SED template (see §3.2 below for more details about the template). We found that a single scaling factor on the IRAC N nuclear fluxes satisfies matching both 5.8 μm and 8.0 μm fluxes with the IRS-synthetic photometries, and the factor is applied to all four IRAC channel fluxes. For the S nucleus, we added scaled IRAC fluxes at the N nucleus to the fluxes at the S nucleus to match IRS-synthetic photometries at the S nucleus. Here we utilized the fact that colors of the N nucleus are very similar to those in the surrounding region of the S nucleus (Figure 2). We calculated the scaling factor by considering, again, both 5.8 μm and 8.0 μm fluxes. We found that a single scaling factor satisfies matching fluxes in both channels, and applied the factor to all four IRAC channels. The adjusted IRAC fluxes for each nucleus are also shown in Table 1. Note that the adjusted fluxes are used only for analyzing MIR SED together with IRS.

2.3. *T-ReCS Spectrum*

The N-band high-spatial low-spectral resolution spectrophotometry of the S nucleus taken by Díaz-Santos et al. (2010a) shows remarkably different signatures just on the nucleus, and we therefore include the data in our analysis. The spectrum was taken with T-ReCS at the Gemini-South Telescope through a 0″.36-wide slit under 0″.35 FWHM seeing condition, providing the best spatial resolution at N band owing to both the diffraction-limited 8 m telescope and the seeing-matched narrow slit. The spectrum is extracted over 0″.36 (or four pixel width) around the peak at the S nucleus. Díaz-Santos et al. (2010a) performed flux calibration by a standard star observation while considering the slit loss effect, and we further applied the aperture correction to estimate the flux of the central compact source by compensating loss of photons outside the extraction aperture box. By assuming a Gaussian PSF of the seeing size, we estimated and multiplied a factor of 1.30 on the original data presented by Díaz-Santos et al. (2010a) in their Figure 3. Since error of the spectrum is not explicitly given, we

estimated it from a scatter of the data points around the fitted model profile (see Figure 3 of Díaz-Santos et al. 2010a).

2.4. *HST NICMOS Images*

In order to extend the shorter wavelength coverage of the nuclear spectrophotometries, we also analyzed high-resolution *HST* NICMOS images at NIR. We retrieved the combined NIC3 images of F110W (1.1 μm wide band), F160W (1.6 μm wide band), and F222M (2.2 μm medium-wide band) from the *Hubble* Legacy Archive. The NIC3 camera provides a larger field-of-view and is good for comparison with the IRAC images. Their spatial resolutions (PSF size in FWHM) are 0$''$26 for all three bands. Flux measurement is based on standard flux conversion factors for the instrument and the filter from the NICMOS Handbook. The *HST* images presented by Lira et al. (2002) and Alonso-Herrero et al. (2002, 2006a,b) are from a different data set taken with the NIC2 camera of the NICMOS instrument. A small correction of tilted background was made for each filter image by fitting the image with a tilted plane while masking sources for each filter band. Astrometry is corrected with three bright field stars in the 2MASS catalog outside of the galaxy, and the global accuracy is about 0$''$2. The F160W and F222M images are shown along with the IRAC images in Figure 1. Zoom-up images of all three filters around the S nucleus are also shown in Figure 4. A compact source marginally appears on the F222M image, although it is blended with surrounding structures. This source is not clearly identified in F160W and F110W. For more NICMOS images for other lines/bands and their descriptions, see Lira et al. (2002) and Alonso-Herrero et al. (2002, 2006a).

3. INFRARED RESULTS

3.1. *Infrared Morphology*

Figure 1 compares overall morphology of the galaxy in all IRAC channels and NICMOS F160W and F222M images. In general, IRAC channels (in particular the longer 5.8 and 8.0 μm channels) trace star-forming regions and the NICMOS bands trace stellar population. The N nucleus is bright and distinct in all IRAC channels. The S nucleus is barely visible at 2.2 μm and is more evident in the IRAC channels. The N nucleus is brighter than the S nucleus at 3.6, 5.8, and 8.0 μm, while the two nuclei are comparable at 4.5 μm. Such characteristics were noted for 2.2, 3.6, 4.5, and 5.8 μm by Lira et al. (2002, 2008). Kotilainen et al. (1996) also showed that both nuclei are equally bright at *L*' band (3.6 μm).

The flux ratios at the S nucleus are remarkably different from the rest due to a compact red source at the S nucleus. The S nucleus shows larger 2.2 μm/1.6 μm and 4.5 μm/3.6 μm, and smaller 5.8 μm/4.5 μm flux ratios than those of the N nucleus and most of the host galaxy (Figure 2). The large-scale dust lanes known around the S nucleus in the optical wavelengths (Zepf et al. 1999; Moran et al. 1999; Lípari et al. 2000; Alonso-Herrero et al. 2002, 2006a; Sakamoto et al. 2014) are not visible in the MIR flux ratio maps. The red S nucleus stands out even more in the *HST* data when the stellar component with complex morphology is subtracted. We modeled the stellar component of the host galaxy in the F222M band

using F160W and F110W images. First we measured stellar colors at each pixel by using the two images, and we then synthesized the stellar F222M image by linearly extrapolating from the F160W image by considering the stellar colors. We scaled the synthesized image by a factor of 0.74 to match the observed F222M image at well outside of the S nucleus. This correction factor is probably due to color corrections on the filters for very red stellar continuum along with the heavy dust lanes around the S nucleus (Zepf et al. 1999; Moran et al. 1999; Lípari et al. 2000; Alonso-Herrero et al. 2002, 2006a; Sakamoto et al. 2014). We found a distinct compact peak at the S nucleus on the F222M image subtracted for its synthetic stellar component (Figure 4), indicating an additional component at the S nucleus. This compact source coincides with the red peak in the F222M/F160W image, a radio continuum source at the S nucleus (e.g., Norris & Forbes 1995; Neff et al. 2003; Sakamoto et al. 2014), and a compact (at 0$''$30 FWHM resolution) 8.74 μm continuum source at the S nucleus (Alonso-Herrero et al. 2006b).

The red compact source at the S nucleus contains an unresolved (at 0$''$26 FWHM, or 44 pc) core. We fitted the source with one and two circular Gaussian components. In the single-Gaussian model, we found a systematic radial variation in the residual map in a sense that the center has a compact positive residual peak and the surrounding region systematically shows negative residuals. In the double-Gaussian model, we assumed that the two Gaussian components share the same center position and that the more compact component is unresolved (at 0$''$26 FWHM). The residual map has much less systematic structure compared with the single-Gaussian model. The reduced χ^2 are 1.8 and 1.0 for the single- and double-Gaussian models, respectively. Therefore, the double-Gaussian model with an unresolved core is preferred. The fitting results are summarized in Table 2.

3.2. *MIR Spectra/SEDs and Color-Based AGN Diagnostics at Individual Nuclei*

The two nuclei are basically similar to each other in the IRS spectra, but we found their noticeable differences. The IRS spectra of both nuclei show prominent PAH and mild silicate absorption features as well as some fine structure lines (Figure 3). Such characteristics are common to LIRGs (e.g., Petric et al. 2011). We compare the observations with the starburst IRS template of Brandl et al. (2006), which was generated by averaging IRS spectra of local starburst galaxies. Since this template is taken with exactly the same instrument and module (SL), we can directly compare it with our observations. Although the template reproduces the observations rather well, we found two notable differences between them. One is the depth of the 9.7 μm silicate absorption, which is characterized by $S_{\mathrm{Si}\ 9.7\ \mu\mathrm{m}} \equiv ln\ (F_\lambda^{\mathrm{obs}}/F_\lambda^{\mathrm{cont}})$. Here, $F_\lambda^{\mathrm{cont}}$ is a continuum flux at 9.7 μm estimated following Díaz-Santos et al. (2010a). We measured $S_{\mathrm{Si}\ 9.7\ \mu\mathrm{m}} = -0.65 \pm 0.20$, -1.31 ± 0.34, and -0.50 for the N nucleus, S nucleus, and the IRS starburst template, respectively. The S nucleus shows significantly deeper absorption than the N nucleus, which shows similar depth within uncertainty as the starburst template. We note that the N nucleus shows slightly smaller $S_{\mathrm{Si}\ 9.7\ \mu\mathrm{m}}$ than the template, although the observed 9.7 μm flux at the N nucleus is larger

than the template scaled at 6.0–8.0 μm (Figure 3). This is because the N nucleus also shows higher continuum at $\gtrsim$ 12 μm than the scaled template due to systematically redder color at $\gtrsim$ 9 μm, and the estimated continuum level at 9.7 μm is also higher for the N nucleus. Another difference is the color at $\lambda \lesssim$ 6 μm. Ratio of our IRS observations to the starburst template (Figure 5) shows a steep excess at the S nucleus below $\simeq$ 6 μm, reaching about data-to-template ratio of $\sim$ 2 at $\simeq$ 5 μm. The N nucleus does not show such a systematic deviation from the template. We also compare the observations with a starburst-powered LIRG SED template of NGC 6090 (log L_{IR} ($L_\odot$) = 11.51; Sanders et al. 2003) from Polletta et al. (2007) (Figure 3). The template was generated to fit the observations with the GRASIL code (Silva et al. 1998), which is a physical starburst evolution model for estimating SEDs. Although this template also roughly resembles the spectra of two nuclei, it seems closer to the N nucleus at < 6 μm.

The IRAC SEDs further illustrate the difference between the two nuclei (Figure 3). At the S nucleus, the IRAC flux monotonically increases toward longer wavelengths, i.e., no flux drop is found at 4.5 μm. At the N nucleus, the IRAC 3.6–4.5 μm color is almost flat, indicating a contribution from the stellar component, which has a blue color at > 1.6 μm (e.g., Sawicki 2002). The slope between 4.5 μm and 8.0 μm is steeper (redder) at the N nucleus than at the S nucleus. An excess flux at 4.5 μm at the S nucleus causes such differences.

By utilizing IRAC color-color diagrams for AGN diagnostics, we found that the S nucleus shows AGN-like SED at 3.6–8.0 μm (Figure 6). Two types of such diagrams have been developed for AGN diagnostics. One is based on flux ratios of 5.8 μm/3.6 μm vs. 8.0 μm/4.5 μm originally proposed by Lacy et al. (2004). We take color boundaries for AGN selection from Donley et al. (2012), who modified the flux ratio cut of 5.8 μm/3.6 μm from the original one. Another is based on 5.8 μm-8.0 μm and 3.6 μm-4.5 μm colors (in magnitudes) proposed by Stern et al. (2005). Although the same IRAC flux information is used in both plots, they are not completely consistent in identifying photometric AGN candidates. The IRAC colors at the S nucleus are in the area for AGNs, which include SEDs of pure power-law and hot blackbody of 300–1000 K. The N nucleus is closer in the IRAC colors to starburst-dominated sources (either spiral galaxies, starbursts, or ultra-luminous infrared galaxies (ULIRGs)). The difference in colors can be again interpreted as due to 4.5 μm excess at the S nucleus.

3.3. *MIR Spectrophotometry Modeling*

It is very likely that the S nucleus is composed of multiple components with different characteristics. This is because the spectrum of the S nucleus at 0$\farcs$36 scale is remarkably different from the spectra at arcsec resolution (Díaz-Santos et al. 2010a). Within the 0$\farcs$36 aperture, the S nucleus shows much deeper silicate absorption without detectable PAH. The PAH features are evident in the IRS at $\sim$ 3$''$ scale (Díaz-Santos et al. 2010a; Pereira-Santaella et al. 2010, this work), the wider-slit T-ReCS (1$\farcs$3-wide; Lira et al. 2008), and the TIMMI2 (1$\farcs$2-wide; Siebenmorgen et al. 2004; Martín-Hernández et al. 2006) spectra. This difference is probably because circumnuclear star-forming regions dominate the MIR flux within the larger

apertures. In terms of flux level, all the larger-aperture spectrophotometries are comparable to our IRAC 8.0 μm nuclear photometry, but the T-ReCS 8.0 μm flux within the 0$\farcs$36 aperture is as small as 30% of the IRAC flux.

We constructed simple composite SED models for the S nucleus with and without AGN to examine how additional AGN contribution can better reproduce the MIR observations compared to a pure (but absorbed) starburst model. We fitted the models to both the high spatial-resolution T-ReCS spectrum, in particular its deep silicate absorption, and the nuclear IRAC and IRS spectrophotometries, in particular its prominent PAH features. For simplicity, only two components are in the composites. One of them needs to be compact and heavily absorbed to reproduce the very deep silicate absorption of the T-ReCS spectrum. Another one represents the extended circumnuclear star-forming region which appears to dominate the PAH feature. We made two such composite models. The AGN-starburst composite model assumes a heavily absorbed AGN in addition to surrounding star-forming regions at $\sim$ 3$''$ scale. The starburst-starburst composite model assumes heavily and mildly absorbed starburst regions. Emission from the heated dusts associated with the compact and heavily absorbed starburst component is not considered in the fitting. As a reference, we also constructed a single-component absorbed starburst model without an AGN. Although Alonso-Herrero et al. (2012) already did similar but more sophisticated SED modeling over the whole aperture IRS spectrum, ours is improved in the following three points. Firstly, we include the IRAC 4.5 μm flux, below the IRS wavelength coverage, in the fitting so that the bluer SED at < 6 μm of the S nucleus can be clearly traced. The IRAC 3.6 μm flux is not included in the fitting because the flux is usually contaminated by stellar emission and relative contribution of the stellar component with respect to non-stellar component varies from one star-forming region to another. Secondly, we utilize the nuclear spectrophotometry. Alonso-Herrero et al. (2012) used a very large aperture IRS spectrum that includes both nuclei and their surroundings. Given the only mild differences between the N and S nuclei at the IRS spatial resolution (§3.2), it is essential to separately analyze the nuclear spectra. Thirdly, we require our model to fit the high-spatial-resolution T-ReCS spectrum while simultaneously fitting the IRAC and IRS spectrophotometry.

We fit the T-ReCS spectrum at 8.0–12.9 μm (§2.3) and the IRAC 4.5 μm–IRS spectrophotometries at 4.5–14.5 μm (§2.2.1). For reference, we also fit only the IRS spectra (5.2–14.5 μm) to evaluate the effect of including the IRAC 4.5 μm photometry. We employed a standard χ^2 minimization technique implemented in the MPFIT software package (Markwardt 2009). For the starburst component, we adopt the LIRG SED template of NGC 6090 from Polletta et al. (2007) since the IRS starburst template of Brandl et al. (2006) does not completely cover the IRAC 4.5 μm channel. For the AGN component, we adopt a pure power-law SED ($f_\nu \propto \nu^\alpha$) with a power-law index (α) of −0.5. The colors/flux ratios of this SED are well within the expected ones for AGNs (Figure 6), and, as we show later, this intrinsically bluer power-law fits the observed IRAC SED when heavily extinct to fit the deep silicate feature of the T-

ReCS spectrum. For the extinction curve, we adopt three different types and compare the results because, as we demonstrate later, a slight difference in silicate absorption profile can result in quite different best-fit parameters with similarly good statistics for the same T-ReCS data. This strongly affects our fit to the IRAC and IRS data covering wider wavelengths. We cannot identify more appropriate extinction curve without having good anchor point(s) of the fit away from the very deep silicate absorption. Due to the same problem, we fit the two sets of spectrophotometry data one by one because fit to the T-ReCS spectrum at 8.0–12.9 μm hardly constrains our fit around 4.5 μm on the IRAC and IRS spectrophotometries. Therefore, we first fit the T-ReCS spectrum with each of the three extinction curves by two SED models (either starburst or AGN). During the fit, we fix the redshift, and fit the SED scaling factor and extinction (represented by optical depth at 9.7 μm, $\tau_{9.7\mu m}$). We then subtract the fitted model from the IRAC and IRS data, and fit the residual spectra with the starburst SED by using the same extinction curve. We again fix the redshift, and fit the SED scaling factor and $\tau_{9.7\mu m}$. We assume a screen geometry for both components. We do not consider an effect of radiation from heated dust, although such a radiation is expected for a compact dusty region surrounding the central energy sources (either starburst or AGN).

We employ the following three extinction curves in the fitting. The first one is a theoretical extinction curve of Chiar & Tielens (2006) (hereafter, CT06) for the Galactic center. The second is from a spectral fitting code PAHFIT (Smith et al. 2007b). Smith et al. (2007b) introduced a hybrid curve consisting of an observed 9.7 μm silicate absorption profile, an empirical 18 μm silicate absorption profile, and a power-law component. The 9.7 μm silicate feature is taken from Kemper et al. (2004) based on the observation toward the Galactic center. This curve is found to work very well on IRS spectra of normal and star-forming galaxies (Smith et al. 2007b; see also, e.g., Díaz-Santos et al. 2010b; Pereira-Santaella et al. 2010; Díaz-Santos et al. 2011). The third one uses the same function of PAHFIT but with a different parameter set to reproduce the updated extinction curve toward the Galactic center by Fritz et al. (2011). The curve of Fritz et al. (2011) shows stronger silicate absorption than that of CT06, although both curves are for the Galactic center. For our fitting purpose, we modified parameters of the PAHFIT extinction curve to reproduce the very high-resolution extinction curve of Fritz et al. (2011). We set the power-law slope of the continuum extinction curve zero, and relative strength of the power-law component with respect to the 9.7 μm silicate feature strength (β; Smith et al. 2007b) 0.155. Because the extinction curve of Fritz et al. (2011) is almost proportional to that of CT06 below the silicate feature, we replaced short side of the extinction curve (< 7.3 μm) with the scaled curve of CT06. This gives smaller $A_{\rm V}/\tau_{9.7}$ (5.8) than that of CT06 ($A_{\rm V}/\tau_{9.7} = 9$). The three extinction curves are compared in Figure 7. Results of the fits are summarized in Figure 8 and Table 3. As we show below, the original PAHFIT extinction curve gives much poorer fits, therefore the best-fit SED models are not shown with this curve in Figure 8.

3.3.1. *Absorbed Single-Starburst Model*

In the absorbed single-starburst model (Figure 8 top), we modeled the IRAC 4.5 μm–IRS spectrophotometry of the S nucleus only with the absorbed LIRG SED template. Although the model reproduces the IRS spectrum reasonably well, neither the 4.5 μm excess nor deep silicate absorption at the 0.″36 scale can be reproduced. Reduced χ^2 are about 4–6 for all three extinction curves, and the IRAC 4.5 μm flux contributes most to the χ^2.

3.3.2. *AGN-Starburst Composite Model*

In the AGN-starburst composite model (Figure 8 middle), we found a good fit, although not statistically satisfactory, to the T-ReCS spectrum with the AGN template by using the extinction curve of CT06 (reduced $\chi^2 = 1.4$) and our modified PAHFIT extinction curve (reduced $\chi^2 = 1.2$). On the other hand, the original PAHFIT extinction curve gives poor fit (reduced $\chi^2 = 3.6$) because the curve always produces asymmetric extinction at both ends of the silicate absorption profile, while the observed profile is more symmetric than the curve. We note that the best-fit parameters are significantly different for different extinction curves ($\tau_{9.7}$=9.4 and 12.7 for the extinction curve of CT06 and our modified PAHFIT extinction curve, respectively). As explained earlier, this is due to slightly different profile of the silicate absorption feature and absence of fit anchor point(s) outside the feature. For the fit to the IRAC 4.5 μm–IRS spectrophotometers, both extinction curve of CT06 (reduced $\chi^2 = 1.4$) and our modified PAHFIT extinction curve (reduced $\chi^2 = 0.8$) resulted in $\tau_{9.7} \simeq 0.5$–0.7. We note that the IRAC 4.5 μm flux dominates the χ^2 in a fit with the extinction curve of CT06 in a sense that the fit under-predicts the observation.

3.3.3. *Starburst-Starburst Composite Model*

In the starburst-starburst composite model (Figure 8 bottom), we found that a heavily absorbed LIRG SED also fits the T-ReCS spectrum (reduced $\chi^2 = 1.2$ for the extinction curve of CT06 and our modified PAHFIT extinction curve). This is because the silicate absorption profile of the extinction curve essentially dominates the shape of the absorbed SED within the T-ReCS wavelength coverage. Again, the original PAHFIT extinction curve gives poor fit (reduced $\chi^2 = 2.7$) because of the same reason for the case of the AGN-starburst composite model. The fits to the IRAC 4.5 μm–IRS spectrophotometries (reduced $\chi^2 \simeq 4$–6) are much worse than those of the AGN-starburst composite model (reduced $\chi^2 \simeq 0.8$–1.4), because contribution to the 4.5 μm flux from the heavily absorbed LIRG template is negligibly small.

3.3.4. *Summary and Implication of the SED Modeling Results*

We found that the AGN-starburst composite model fits the MIR observations much better than the starburst-starburst composite model since AGN contribution can reproduce the 4.5 μm excess. In particular, the modified PAHFIT extinction curve gives better fit to the 4.5 μm flux, and we prefer the results with this extinction curve, i.e., Figure 8 right-middle. This model can also roughly

explain the NICMOS 2.2 μm flux of the unresolved nuclear component, although the flux is not included in the fit (Figure 9). In our best-fit model with the modified PAHFIT extinction curve, the AGN contributes $\simeq 24\%$ and $\simeq 2\%$ of the 6 and 24 μm fluxes, respectively. As for the optical depth on the AGN component, we use both results, $\tau_{9.7} = 9.4 \pm 0.4$ and 12.7 ± 0.5 from the extinction curve of CT06 and our modified PAHFIT extinction curve, respectively, and adopt the possible range of the optical depth of $\tau_{9.7} = 9$–13, since the two extinction curves provide statistically equally good fit to the T-ReCS spectrum.

We estimate the column density toward the AGN to be on the order of $N_{\mathrm{H}} \sim 10^{23}$ cm^{-2}. We assumed a screen geometry of the dusty region. The optical depth at 9.7 μm over the AGN continuum, $\tau_{9.7} = 9$–13, corresponds to $A_{\mathrm{V}} \sim 80$ mag by using the conversion factors of $A_{\mathrm{V}}/\tau_{9.7} = 9$ and 5.8 for extinction curves of CT06 and our modified PAHFIT, respectively. Further assuming a standard conversion factor for the solar neighborhood, $N_{\mathrm{H}}/A_{\mathrm{V}} = 1.9 \times 10^{21}$ cm^{-2} mag^{-1} (Bohlin et al. 1978), the neutral Hydrogen column density toward the AGN is estimated to be $N_{\mathrm{H}} \simeq 1.5 \times 10^{23}$ cm^{-2}.

We can also estimate the star formation rate (SFR) and IR luminosity of the S nucleus. By subtracting the synthetic 8.0 μm flux of the AGN component (16 mJy), we estimate 8 μm flux from the starburst component of our best AGN-starburst composite model is 35 mJy. We then estimate SFR to be 0.43 M$_\odot$ yr^{-1} by using calibration of Zhu et al. (2008), which is derived for young (10–100 Myr continuous burst) starburst with Salpeter initial mass function (0.1–100 M$_\odot$) based on IR (8–1000 μm) luminosity–SFR conversion and monochromatic 8 μm luminosity–IR luminosity correlation. This SFR corresponds to $L_{\mathrm{IR}} \simeq 2.5 \times 10^9$ L$_\odot$. Zhu et al. (2008) noted that correlation between MIR and IR luminosities are essentially the same for AGN-starburst composite galaxies, AGNs, and star-forming galaxies. Therefore, the IR luminosities of the AGN and the S nucleus, including the AGN and the circumnuclear starburst component, are estimated to be $\simeq 1.1 \times 10^9$ L$_\odot$ and 3.6×10^9 L$_\odot$, respectively[2]. We note that the AGN luminosity is highly uncertain because the correlation between the MIR and IR luminosities is established for field AGNs found in a blank-sky survey (Zhu et al. 2008), and it is not clear if the same correlation applies to the heavily absorbed AGN at the S nucleus. For comparison, the IR luminosity of the N nucleus estimated in the same way from the observed 8.0 μm flux is $\simeq 1.5 \times 10^{10}$ L$_\odot$. The total infrared luminosity at 3–1100 μm (TIR) of the N nucleus is also estimated from the whole-aperture TIR luminosity by Engelbracht et al. (2008), who used both IRAC and MIPS (Rieke et al. 2004) 24 μm, 70 μm, and 160 μm fluxes. Since the IRAC colors of the N nucleus are very similar to that of the rest of the galaxy, and the S nucleus that shows distinct colors consists of only a few percent of the whole aperture flux (§2.1), we scale the whole-aperture TIR luminosity according to the nuclear fluxes at 8.0 μm. We then found $L_{\mathrm{TIR}} = (2.0$–$2.4) \times 10^{10}$

---

[2] Sakamoto et al. (2014) referred to this paper in its submitted form for the FIR luminosities. The quoted luminosities are $\simeq 2.9 \times 10^{10}$ L$_\odot$, $\simeq 1.5 \times 10^{10}$ L$_\odot$, and $\simeq 5.0 \times 10^9$ L$_\odot$ for the N nucleus, the S nucleus, and the AGN in the S nucleus, respectively. During the revision of this paper, we revised the numbers as shown here.

L$_\odot$ for the N nucleus.

4. X-RAY DATA

We analyzed archival data of two *Chandra* observations of NGC 3256 to search for X-ray indications of the presence of an AGN in the S nucleus. The superb spatial resolution of *Chandra* enables us to extract X-ray spectrum of the S nucleus separated from other emission components in the host galaxy. The two *Chandra* observations are summarized in Table 4. The observations performed on 2000 Jan 5 and 2003 May 23 are referred to as the first and second observations, respectively, hereafter. NGC 3256 was located on the back illuminated CCD chip ACIS-S3 in both observations. The *Chandra* Interactive Analysis of Observations (CIAO) software package version 4.6 combined with the latest calibration database (CALDB) version 4.6.3 was used to analyze the *Chandra* data. The data were reprocessed to generate level=2 event files using the latest calibration.

We made a light curve for a source free region in the same CCD chip to examine the stability of background and discarded time intervals showing high background. The background was stable in the second observation, while the background rates were relatively high in the first. The resulting exposure times after discarding high background intervals are 16.2 and 27.2 ksec for the first and second observations, respectively, totaling $\simeq 2.7$ times more exposure time than that in Lira et al. (2002). X-ray spectra of the S nucleus were extracted using a circular region with a radius of 2.2 pixels or 1$''$1. Background spectra were made using a circular region with a radius of 5$''$2 (first observation) or 5$''$9 (second observation) that does not contain noticeable point sources near NGC 3256 and were subtracted from the source spectra. The net counts after the background subtraction are shown in Table 4 and the background subtracted spectra are presented in Figure 10. The spectra of the S nucleus were binned so that each bin contains at least one count.

Spectral fits were performed by using XSPEC version 12.8.2. We applied a maximum likelihood method to fit the spectra using the modified version of C statistic (Cash 1979), in which a Poisson distribution is assumed for numbers of counts in each bin. While the absolute value of C does not provide goodness of fits, ΔC can be used to examine relative goodness or to generate confidence intervals. The errors are at the 90% confidence range for one parameter of interest ($\Delta C = 2.7$). The Galactic absorption $N_{\mathrm{H}} = 9.35 \times 10^{20}$ cm^{-2} (Kalberla et al. 2005) calculated by using the tool `nh` in FTOOLS was applied to all the models examined below. The `phabs` model in XSPEC was used for photoelectric absorption, in which the cross sections from Balucinska-Church & McCammon (1992) with a He cross section in Yan et al. (1998) are used. All the spectral components except for the Galactic absorption were assumed to be emitted/absorbed at the source redshift.

5. X-RAY RESULTS

We fitted the spectra from the two observations simultaneously. Since the photon statistics are limited, we assumed same spectral parameters for the two spectra. A constant factor was multiplied to the model to represent variability between the two observations. This factor was fixed at unity for the first observation and left free for

the second observation.

5.1. *Power-Law Models*

A simple power law modified by absorption intrinsic to the source (model A) was examined first. The resulting parameters are summarized in Table 5, and the photon index and absorption column density of $-0.42^{+0.67}_{-0.27}$ and $< 9.7 \times 10^{21}$ cm^{-2} (90% confidence upper limit), respectively, were obtained. Although this model represents the overall shape of the spectra, the best-fit photon index is extremely flat. If the photon index is fixed at a steeper value 1.8, which is typically observed in Seyfert galaxies (e.g., Dadina 2008), the C statistic becomes worse by $\Delta C = 17.7$ (Model B).

An apparently flat spectrum is often explained by a reflection dominated spectrum or a combination of heavily absorbed and lightly absorbed continua, and these possibilities are tested below. The former case is expected if the primary X-ray emission is obscured by a large amount of matter exceeding a column density of $\sim 10^{24}$ cm^{-2} and if emission scattered by medium surrounding the X-ray source dominates observed spectra. In oder to represent a spectrum dominated by reflection by cold matter, the `pexrav` model (Magdziarz & Zdziarski 1995) in XSPEC modified by intrinsic absorption was used. The incident spectrum was assumed to be power law with an exponential high energy cutoff. The photon index and the cutoff energy were fixed at 1.8 and 300 keV, respectively, since these parameters were not well constrained from the observed spectra. A reflector of a slab shape with an inclination angle of 60° was assumed, where 0° corresponds to face on. The abundance of the reflector was assumed to be solar, where the abundance table of Anders & Grevesse (1989) was used. The reflection normalization factor ("`ref_refl`" parameter) was fixed at -1 so that only the reflected continuum emission is obtained. This model (Model C) represents the observed spectral shape, and the best-fit parameters are shown in Table 5, though the absence of Fe-K emission line is not compatible with this refection dominated model as discussed in §6.1.2.

Another possibility to explain the very flat continuum is a multicomponent model consisting of heavily and lightly absorbed continua. We assumed a power law continuum with a fixed photon index of 1.8 as an incident spectrum and the absorption column densities of $N_{\rm H,1}$ and $N_{\rm H,2}$ for light and heavy absorbers, respectively. This model is expressed as $e^{-\sigma(E)N_{\rm H,1}} \, [f e^{-\sigma(E)N_{\rm H,2}} + (1-f)] \, A \, E^{-\Gamma}$, where E, $\sigma(E)$, f, A, and Γ are photon energy, photoelectric absorption cross section, fraction of continuum emission absorbed by $N_{\rm H,2}$, normalization of power law, and photon index, respectively (Model D). The observed spectra are well represented by this model. The result of this fit is also in Table 5. The best-fit model is shown in Figures 10 and 11. The measured column density of the heavy absorber ($7^{+19}_{-3} \times 10^{22}$ cm^{-2}) is consistent with the MIR measurement of an AGN absorption from the AGN-starburst composite model ($\simeq 1.5 \times 10^{23}$ cm^{-2}) (§3.3.4).

The constant factors multiplied to the models obtained from the fits are summarized in Table 5. The best-fit values for the models examined above are in the range from 0.92 to 0.95, and the error ranges contain unity. There-

fore, flux variability between the two observations is not significant. Observed fluxes and luminosities corrected for absorption in the 2–10 keV band are also shown in Table 5 except for the model B, for which C statistic was significantly worse than those for other models.

The observed spectra do not show an indication of an Fe-K emission line. We calculated an upper limit on the EW of a fluorescent Fe-K line at 6.4 keV by adding a Gaussian spectral component to the models examined above. The center energy was fixed at 6.4 keV. The line width σ is assumed to be 10 eV, since previous observation of type 2 AGNs show that Fe-K line width is much narrower than the energy resolution of ACIS (Shu et al. 2011). The upper limit on the line EW is shown in Table 5.

5.2. *Thermal Emission Models*

We also examined a thermal emission model. The APEC model (Smith et al. 2001) was used as emission from optically-thin plasma in collisional ionization equilibrium. A combination of multiple components, one of which is heavily absorbed, is required to explain the apparent flat spectrum. We therefore examined a model consisting of unabsorbed and absorbed APEC components represented by the expression $\mathtt{apec}(T_1) + e^{-\sigma(E)N_{\rm H}} \, \mathtt{apec}(T_2)$, where T_1 and T_2 are temperatures for unabsorbed and absorbed APEC components, respectively (Model E). Only lower bounds for allowed temperature ranges for these two components were obtained as 1.2 keV and 9.4 keV, respectively. The intrinsic column density for the absorbed component was obtained to be $N_{\rm H} = 5.1^{+3.3}_{-1.9} \times 10^{22}$ cm^{-2}. This model resulted in the value of C statistic 77.6 for 88 degrees of freedom and describes the shape of the observed spectra, where the plasma temperatures kT_1 and kT_2 were pegged at 64 keV. X-ray spectra of starburst galaxies generally show emission from thermal plasma with a temperature $kT = 1$ keV or less (Ptak et al. 1999; Strickland et al. 2004; Tüllmann et al. 2006), and the high temperatures obtained from the fits are unusual. We therefore examined whether the presence of low temperature ($kT < 1$ keV) plasma is consistent with the observed spectrum by multiplying extra absorption to the model examined above. This trial model is expressed by $e^{-\sigma(E)N_{\rm H,1}}[\mathtt{apec}(T_1) + e^{-\sigma(E)N_{\rm H,2}} \, \mathtt{apec}(T_2)]$, and we found that kT_1 of 1 keV or less is allowed for the component representing the low energy part of the spectra (Model F). If $kT_1 = 1$ keV is assumed, the best-fit $N_{\rm H,1}$ is 1.3×10^{22} cm^{-2}, and $C = 77.3$ is obtained for 88 degrees of freedom. The resulting spectral parameters, observed fluxes, and absorption corrected luminosities for the thermal models are summarized in Table 6.

6. DISCUSSION

6.1. *Evidence of AGN in the S Nucleus*

6.1.1. *In Infrared*

The IRAC colors at the S nucleus indicate a non-starburst-like SED (§3.2). Specifically, the excess of the 4.5 μm flux makes 8.0 μm/4.5 μm flux ratio smaller and [3.6]−[4.5] color larger in both diagnostic diagrams in Figure 6, bringing the S nucleus away from starburst-dominated galaxies in the observed colors. Such col-

ors are found only at the S nucleus in the IRAC images (§3.1). The MIR spectrum of the flux ratio between the two nuclei (Figure 5a) can be used to examine presence of an AGN in a way least dependent on the SED templates. It shows a complicated trend of both the excessed 4–6 μm flux and the deeper 9.7 μm absorption at the S nucleus. The ratio changes in a way different from the dust extinction curves (Figure 7) and, therefore, the two nuclei must have different intrinsic SED shapes. This conclusion is independent of the detailed shape of the extinction curve. Such an excess at 4–6 μm cannot be reproduced only from starburst-dominated SEDs because the observed 8.0 μm/4.5 μm flux ratio is smaller than, and the observed [3.6]−[4.5] color is larger (redder) than, those of starburst-dominated galaxies (Ruiz et al. 2010). We demonstrated with our AGN-starburst composite SED model that the AGN contribution can reproduce the observed 4.5 μm enhancement (§3.3.4).

We discovered a very compact 2.2 μm source at the S nucleus, and its unresolved core (at 0$.\!\!''$26 FWHM) seems a NIR counterpart of the compact (at 0$.\!\!''$30 FWHM resolution) MIR core (Alonso-Herrero et al. 2006b). The 2.2 μm core coincides with the compact MIR and radio sources at the S nucleus (§3.1). Both the 2.2 μm core and the MIR core show a comparable source size. Although this 2.2 μm component is not included in our SED fitting together with the T-ReCS spectrophotometries, the heavily extinct power-law AGN SED that is fitted to the MIR data roughly predicts the 2.2 μm flux (§3.3.4). Therefore, it is very likely that the same power-law component, or hot blackbody-dominated component (see below), dominates the NIR–MIR SED of the nucleus at < 50 pc scale.

Although our SED model fitting prefers a model with AGN, the nuclear IRAC colors can be also represented by a blackbody of $\simeq$ 600 K (Figure 6). Although we neglected dust emission in our SED modeling of the starburst-starburst composite model (§3.3), such dust emission might dominate the SED around 4.5 μm to account for the 4.5 μm excess. Verley et al. (2007) studied SEDs of embedded star-forming regions by considering hot dusty shell with radiative-transfer calculation with *DUSTY* code (Ivezic & Elitzur 1997). No PAH emission is considered within *DUSTY*. The young star clusters are modeled with the *starburst99* (Leitherer et al. 1999) stellar-population model. Among the parameter space they explored, which was designed to cover a range of typical extragalactic H II regions, the S nucleus is closer in IRAC colors to cases of temperature of the inner surface of the dusty shell $T_{\rm in}$ = 600 K and total visual extinction $A_{\rm V}$ = 46.4 mag. A heavy 9.7 μm silicate absorption is also reproduced when the extinction is very high ($A_{\rm V} \sim$ 100 mag). In such configurations of the dusty shell, large extinction suppresses stellar SED at 3.6 μm, and the color becomes similar to a pure blackbody of T = 600 K. Luminosity of the 600 K blackbody component is $\sim 3 \times 10^8$ L$_\odot$ if the blackbody dominates the observed nuclear IRAC SED. If we assume a shell of dusts emitting such blackbody, radius of the shell is < 0.1 pc.

MIR SEDs with dominating hot blackbody are unusual for star-bursting galactic nuclei. Some types of star-forming objects are known to show SEDs similar to the IRAC SED at the S nucleus, but they are likely not responsible for the S nucleus for the following reasons. Hot blackbody-dominated SEDs are found in blue compact dwarf galaxies (Hunt et al. 2005) and ultra-compact H II regions (e.g., Churchwell 1990, 2002). In blue compact dwarf galaxies, vigorous star formation is clearly seen in optical wavelength, and the MIR SEDs resemble a blackbody because of lack of prominent PAH emission due to low metallicity. Because the S nucleus is most likely a nucleus of a massive disk galaxy under merging process (e.g., English et al. 2003; Sakamoto et al. 2014) and the metallicity of the nuclear region is about solar (e.g., Storchi-Bergmann et al. 1995; Lípari et al. 2000), the same explanation for blue compact dwarf galaxies unlikely applies to the S nucleus. In addition, typical X-ray luminosity of such galaxies is about a few 10^{39} erg s^{-1} (Kaaret et al. 2011; Thuan et al. 2014), which is about an order of magnitude fainter than the observed luminosity of the S nucleus. Ultra-compact H II regions are manifestations of newly formed massive stars that are still embedded in their natal molecular cloud, and hence dusty cocoon (Churchwell 1990). It is compact (<1 pc) and emits mostly at infrared from hot dust heated by central O star. Strong silicate 9.7 μm absorption is sometimes seen. Although they are among the most luminous FIR sources in the Galaxy and their MIR spectral characteristics are similar to those of the S nucleus, even the most luminous ultra-compact H II regions in a classical sample of Wood & Churchwell (1989) are $\sim 4 \times 10^3$ times less luminous than that of the S nucleus at $\sim$ 10 μm. Their X-ray luminosities (typically a few 10^{33} erg s^{-1}; Tsujimoto et al. 2006) are also much fainter than the observed luminosity of the S nucleus. Nuclear starburst galaxies and (U)LIRGs hardly show such hot dust component (Marshall et al. 2007; Armus et al. 2007; da Cunha et al. 2010). In a sample of representative local star-forming ULIRGs, da Cunha et al. (2010) requires no component hotter than 250 K in their UV-FIR SED fitting. Armus et al. (2007) pointed out from their detailed analysis of the infrared (1–1000 μm) SEDs for local ULIRGs with and without AGNs that detection of hot dust at $T \gtrsim$ 300 K in a nuclear spectrum provides indirect evidence for a buried AGN.

In summary, our infrared analysis strongly prefers presence of an AGN at the S nucleus. In order to better constrain the nuclear activities, sophisticated SED decomposition as Marshall et al. (2007) did or physical SED modeling with dust radiation-transfer consideration would be necessary. Additional high spatial-resolution photometry data to fill a wavelength gap between NICMOS and N band as well as spatially-resolved photometry of the S nucleus at longer infrared wavelength would greatly help such modeling and analysis.

6.1.2. *In X-Ray*

Chandra imaging of NGC 3256 shows an X-ray source at the position of the S nucleus. Its spatial extent is consistent with the PSF of *Chandra* (Lira et al. 2002). We first discuss possible origins of the X-ray emission assuming that X-rays are coming from one point source. The X-ray spectra are extremely hard; if a simple power law model modified by intrinsic absorption is applied, the best-fit photon index of −0.43 is obtained (Model A). Such a flat spectrum is unusual for primary X-ray emission and suggests a contribution of reprocessed and/or

absorbed emission. If the primary source is hidden behind optically thick matter with a column density greater than $N_H \sim 10^{24}$ cm^{-2} and the observed spectrum is dominated by emission scattered by cold matter, the resulting spectrum becomes very hard. Such a spectrum is referred to as reflection dominated. This situation is observed in Compton-thick AGNs, for which an absorption column density exceeds 1.5×10^{24} cm^{-2} (e.g., Comastri 2004). In this case, a strong fluorescent Fe-K emission line with an EW greater than ~ 700 eV is seen (e.g., Guainazzi et al. 2005; Fukazawa et al. 2011). The observed spectra, however, do not show an indication of Fe-K emission line, and the upper limit on the EW is 190 eV (for model C). This limit is inconsistent with a reflection dominated spectrum and the presence of a Compton-thick nucleus is ruled out.

A dual absorber model (Model D) also provided a good description of the spectrum. Such spectra are seen in AGNs obscured by Compton-thin matter. The fraction, $f = 0.94$, of the continuum absorbed by a large column density (7×10^{22} cm^{-2}) is in the range typically observed in Seyfert 2s (Turner et al. 1997; Noguchi et al. 2010). The less absorbed emission component is often interpreted as emission scattered by ionized medium in the opening part of the putative obscuring torus (e.g., Turner et al. 1997). The upper limit on the EW of an Fe-K emission line (550 eV) is consistent with that expected for the absorption column density of 7×10^{22} cm^{-2} (EW$\simeq$ 50–150 eV; Turner et al. 1997; Guainazzi et al. 2005; Fukazawa et al. 2011). The luminosity in the 2–10 keV band corrected for absorption is estimated to be 1.5×10^{40} erg s^{-1}. The error on the absorption column density introduces uncertainties in the correction of absorption, and the allowed range for the 2–10 keV luminosity is $(1.2$–$2.9) \times 10^{40}$ erg s^{-1}. This luminosity is in the range for low-luminosity AGNs (e.g., Ho et al. 2001; Terashima et al. 2002; Cappi et al. 2006). Thus the observed properties are in accordance with a low-luminosity AGN obscured by Compton-thin matter.

The luminosity of the X-ray source at the S nucleus is much higher than that of a single X-ray binary containing a stellar mass black hole or a neutron star. If the X-ray source is a single compact object, its mass should be greater than

$$1000 M_\odot \left(\frac{1.0}{\lambda_{\rm Edd}} \right) \left(\frac{\kappa_{2-10 \text{ keV}}}{10} \right) \left(\frac{L_{2-10 \text{ keV}}}{1.5 \times 10^{40} \text{ ergs}^{-1}} \right),$$

where $\lambda_{\rm Edd}$, $\kappa_{2-10 \text{ keV}}$, $L_{2-10 \text{ keV}}$ are the Eddington ratio, bolometric correction factor, and intrinsic luminosity in 2–10 keV, respectively. Note that we assumed an Eddington luminosity of 1.5×10^{38} erg s^{-1} for one solar mass, which is based on an assumption of a Hydrogen-to-Helium ratio of 0.76:0.23 by weight. The bolometric correction factor $\kappa_{2-10\text{keV}}$ is known to be dependent on a luminosity and an Eddington ratio. Studies of AGN SEDs show that $\kappa_{2-10\text{keV}}$ is 10–20 for low-luminosity AGNs accreting at an Eddington ratio of <0.1 (Vasudevan & Fabian 2009; Ho 2008).

The X-ray fluxes of the S nucleus for the two observations with a 3 year interval are consistent with each other within errors. A systematic analysis of AGN X-ray light curves of a large sample shows that a high percentage of low-luminosity AGN do not show significant variability (González-Martín & Vaughan 2012), and the absence of variability is consistent with X-ray emission being from a low-luminosity AGN. On the other hand, the absence of variability might be explained by the possibility that the X-ray emission comes from multiple sources. If there are tens of stellar mass black holes well within the size of the PSF of *Chandra* (0''.49 or 83 pc at the distance of NGC 3256), the luminosity measured could be explained. The very hard spectra observed, however, are not compatible with any spectral states of stellar mass black hole binaries (McClintock & Remillard 2006; Done et al. 2007) and superposition of X-ray spectra suffering from different absorption column densities is required. A large number of X-ray binaries are expected in starburst galaxies. The integrated luminosity of high mass X-ray binaries, which have a hard X-ray spectrum, formed by starburst activity is related to SFR (Ranalli et al. 2003; Grimm et al. 2003; Gilfanov et al. 2004). The scaling law of Grimm et al. (2003) between SFR and integrated X-ray luminosity ($L_{2-10 \text{ keV}}$) for low SFR values (< 4.5 M$_\odot$ yr^{-1}) predicts $L_{2-10 \text{ keV}}$ of 6×10^{38} erg s^{-1} for SFR of $\simeq 0.43$ M$_\odot$ yr^{-1} (§3.3.4). The observed luminosity is about a factor of ~ 20 larger than this expectation. *Chandra* images of nearby starburst galaxies indeed show many point sources (e.g., Griffiths et al. 2000; Strickland et al. 2000; Bauer et al. 2001). Such point sources, however, are distributed over a region of several hundreds of parsecs, which is much larger than the limit on the source size of the S nucleus. A single nuclear source is therefore more conceivable, although the possibility of superposition of multiple sources cannot be completely excluded.

A two component thermal plasma model also explains the shape of the observed spectra (§5.2). Thermal plasma emission with a temperature lower than ~ 1 keV is commonly observed in starburst galaxies (e.g., Strickland et al. 2004). Such a component is extended to the scale of host galaxy and intrinsic absorption is generally small. Our spectral fit indicates that emission from plasma with $kT < 1$ keV should be significantly absorbed by a column density of 1.3×10^{22} cm^{-2} or higher if such a component exists. Thus the observed properties are unusual to be interpreted as starburst galaxies in terms of the small source size and low-kT plasma confined and hidden behind absorbing matter.

6.1.3. *Arguments at Other Wavelengths*

In addition to our MIR and X-ray evidence for the AGN, recent radio and NIR observations also suggest the AGN activity in the S nucleus. Sakamoto et al. (2014) found a highly collimated bipolar jet-like outflow of molecular gas from the S nucleus using *ALMA*. It extends up to 4'' (700 pc) from the nucleus and is associated with a bipolar spur of radio continuum emission. They inferred from the morphology and kinematics of the molecular outflow and from the radio feature a jet-driving AGN in the S nucleus. They also found that the continuum spectral slope at 860 μm is flatter at the S nucleus than at the N nucleus. More synchrotron emission from an AGN in the S nucleus would explain the difference. Similar bipolar outflow from the S nucleus was also detected in the NIR H_2 1–0 $S(1)$ line by Emonts et al. (2014), and was suggested to be AGN-driven from the

energetics and high-mass loading factor.

In addition to the X-ray to MIR SED (Lira et al. 2002; see also §6.3 below), the X-ray to radio SED has been used to distinguish types of nuclear activities because these wavelengths are least sensitive to extinction and contamination by stellar activities is minimal there (Terashima & Wilson 2003). Neff et al. (2003) found the ratio of 6 cm radio to 2–10 keV X-ray luminosities, R_X ($= L_R/L_X = \nu L_\nu$ (5 GHz)$/L_{2-10\ keV}$)$= 1 \times 10^{-2}$, for the compact source in the S nucleus from their *VLA* observations and the *Chandra* X-ray results of Lira et al. (2002). By comparing with the ratios of various kinds of Galactic and extragalactic sources, they argued that the compact source is most likely a low-luminosity AGN, although a possibility of a collection of supernova remnants cannot be rejected. Our new X-ray luminosity is only 26% larger than that of Lira et al. (2002), and the revised R_X remains in the range of low-luminosity AGNs as Neff et al. (2003) discussed.

6.2. *Distribution of Dusty Material in and around the S Nucleus*

Our absorption magnitude and column density toward the AGN in the S nucleus, $A_V \sim 80$ mag and $N_H \sim 10^{23}$ cm^{-2}, are much larger than previous estimates at NIR–MIR wavelengths. They are $A_V = 5.3$ and 10.7 mag from the $JHK'L'$ continuum and line photometries, respectively (Kotilainen et al. 1996), 16 mag from the *HST* NICMOS H–K nuclear color measurement (Lira et al. 2002), and 15 ± 5 mag from the *HST* NICMOS line flux ratio (Alonso-Herrero et al. 2006a). Also, Lira et al. (2008) estimated $A_V \sim 10$ mag on the basis of MIR SED fitting within $3''.6$–$4''.0$ apertures. It seems that the previous measurements of $A_V = 5$–15 mag (i.e, $N_H \sim 10^{22}$ cm^{-2}) correspond to the extended dust lanes over 1 kpc scale (e.g., Zepf et al. 1999; Moran et al. 1999; Lípari et al. 2000; Alonso-Herrero et al. 2002, 2006a; Sakamoto et al. 2014) or dusty circumnuclear star-forming region (§3.3). In our MIR SED analysis, we applied mild extinction corresponding to $A_V \simeq 5$–8 mag on the starburst component of the AGN-starburst composite model (§3.3.2). This component is most likely spatially extended because Alonso-Herrero et al. (2006b) reported a slightly extended structure in a $0''.30$ FWHM resolution (51 pc) image of the S nucleus at 8.74 μm. We also found a slightly extended component, besides an unresolved core, in the NICMOS 2.2 μm image ($0''.75$ FWHM or 128 pc) (§3.1). In our X-ray analysis, we showed that the lightly absorbed component of the dual-component model suffers from $N_{H,1} = 0.34^{+1.56}_{-0.25} \times 10^{22}$ cm^{-2} (§5.1), matching the values from previous and our measurements at NIR–MIR. Additional heavy extinction on the AGN is required to account for both the deep silicate absorption at the $0''.36$ scale and the heavy absorption on another component of the dual-component model in the X-ray analysis. Such a heavily absorbed region is most likely within the central $\lesssim 0.5''$ of the S nucleus. At MIR, the silicate absorption becomes much shallower at arcsec scale (Díaz-Santos et al. 2010a; §3.3). At X-ray, high spatial-resolution *Chandra* spectra show that the column density on a heavily absorbed component ($N_{H,2} = 7^{+19}_{-3} \times 10^{22}$ cm^{-2}) is much larger than that on the power-law component in the whole-aperture *XMM-Newton* spectrum ($0.14 \pm 0.03 \times 10^{22}$ cm^{-2}; Pereira-Santaella et al. 2011). For comparison, from high spatial-resolution *ALMA* molecular-gas imaging, Sakamoto et al. (2014) obtained a column density of $N_H = 10^{23}$–10^{24} cm^{-2} to the S nucleus in their $0''.5$ (80 pc) beam.

Both MIR and X-ray analyses strongly suggest that large amount of dusts distributes immediately around the AGN in a form of thick and smooth shell or torus. ULIRGs generally show deeper silicate absorption ($S_{9.7\mu m} \ll -1$) than in AGNs (e.g., Hao et al. 2007), and such deep absorption requires that the energy source is deeply embedded in dust that is both optically and geometrically (along radial direction) thick, as well as geometrically smooth (Levenson et al. 2007; Nenkova et al. 2008a,b; Sirocky et al. 2008). For example, slab geometry cannot make the absorption $S_{9.7\mu m} < -1.1$ even with $\tau_V = 1000$, because one needs temperature gradient within the dusty region and the illuminated surface of the dust should be hidden from our direct views (Levenson et al. 2007). Also, clumpy medium cannot make the absorption very deep because illuminated surface of individual clumps can be directly seen/illuminate dark surface of other clumps (Nenkova et al. 2008a,b). The observed upper limit of the silicate absorption depth at the $0''.36$ resolution, $S_{9.7\mu m} < -3$ (Díaz-Santos et al. 2010a), where the bottom of the feature was not determined due to very strong absorption and the sensitivity, is already in the range of the most heavily absorbed sources in the local universe (Hao et al. 2007). Our MIR SED analysis implies a much deeper depth ($S_{9.7\mu m} = -9$ – -13 where $S_{9.7\mu m} \equiv -\tau_{9.7}$ in our assumed geometry). This strengthens a need for optically and geometrically thick dusty region immediately surrounding the AGN. On the other hand, our X-ray spectrum analysis with a dual-component model suggests that a classical picture of type-2 AGNs with a dusty torus immediately surrounding a supermassive black hole (e.g., Antonucci 1993) applies to the S nucleus. Firstly, the elevated column density at the S nucleus is compatible with a typical dusty torus of Compton-thin type-2 AGNs (e.g., Awaki et al. 1991; Turner et al. 1997; Guainazzi et al. 2005; Fukazawa et al. 2011). Secondly, the model also suggests that $\simeq 6\%$ of the primary X-ray spectrum is seen unabsorbed by the heavy absorber, and this component can be interpreted as emission scattered by ionized medium in the opening part of the putative obscuring torus around the AGN. Such phenomenon is commonly seen in typical Seyfert 2s (Turner et al. 1997; Noguchi et al. 2010). To reproduce deep silicate absorption with such a torus, the torus must be geometrically thick enough along the height direction, as well as along the radial direction, or our viewing angle must be close enough to the equatorial plane of the torus, so that the inner illuminated surface is hidden from our line-of-sight.

6.3. *Revisiting X-Ray-to-MIR SED*

The S nucleus is known to be X-ray-quiet, and the fact has been considered to be evidence against an AGN there (Lira et al. 2002), although the galaxy as a whole is among the most luminous X-ray sources without confirmed AGN in the local universe (Moran et al. 1999; Lira et al. 2002; Pereira-Santaella et al. 2011). Lira et al. (2002) revealed a compact X-ray source at the S nucleus with the first *Chandra* observation and reported the

neutral Hydrogen column density obscuring the nucleus to be $N_H = 5 \times 10^{22}$ cm^{-2} (best fit)–1×10^{23} cm^{-2} (acceptable). By using a radio–FIR–MIR-X-ray SED of the S nucleus, Lira et al. (2002) showed that the observed X-ray luminosity is higher than that of typical starbursts but is at least two orders of magnitude lower than expected for a classical Seyfert nucleus. Alexander et al. (2005) plotted the data of Lira et al. (2002) for the total aperture in the correlation diagram between IR and (absorption-corrected) X-ray luminosities together with well-studied local starbursts and AGNs. They demonstrated that the X-ray luminosity of NGC 3256 between 0.5 keV and 8 keV is well below the range of AGNs but the galaxy is slightly more X-ray luminous than the starburst galaxies.

Our AGN-starburst composite model indicates that the observed SED is heavily contaminated at MIR by the circumnuclear star formation, and we found that the AGN component alone is consistent with typical AGNs in terms of X-Ray-to-MIR SED. Horst et al. (2006, 2008) demonstrated that contamination by the circumnuclear starburst at MIR must be removed when evaluating AGN SEDs. By using high spatial-resolution MIR photometries, Horst et al. (2006, 2008) and Gandhi et al. (2009) showed that the ratio of the MIR luminosity at 12.3 μm to the absorption-corrected X-ray luminosity at 2–10 keV scatters within a range of $\log L_{12.3\ \mu m}/L_{2-10\ keV} = -0.5$ to 1.5, with a mean of 0.61 ± 0.31 among both type-1 and -2 Seyfert nuclei. In the case of the S nucleus, we adopt the T-ReCS flux at 12.3 μm within the $0''.36$ aperture (Díaz-Santos et al. 2010a) and the absorption-corrected X-ray luminosity of the dual-component model (Model D; §6.1.2). Then we find $\log L_{12.3\ \mu m}/L_{2-10\ keV} \sim 0.8$–1.2 ($= 1.1$ with the best-fit 2–10 keV luminosity) for the AGN in the S nucleus. It is in the range of ratios that Horst et al. (2008) and Gandhi et al. (2009) obtained for Seyfert nuclei. Therefore, we conclude that the apparent X-ray quietness of the S nucleus should no longer be considered as evidence against AGN in the nucleus.

6.4. *Comparison with Previous Results*

Although our conclusion of the presence of an AGN in the S nucleus appears contradictory to most of the earlier studies, they are consistent with each other if we consider different aperture sizes and contamination from circumnuclear star formation. Lira et al. (2002, 2008) noted the 4.5 μm excess at the S nucleus among the three IRAC channels. Lira et al. (2002) also noted, by adding information of ground-based $JHK'L'N$-band photometry, that the S nucleus is in the 1–10 μm SED in νF_ν flatter than typical starburst galaxies and is closer to AGNs. However, they concluded that the AGN contribution is insignificant, if any. This is because in Lira et al. (2002) their FIR–MIR–X-ray SED for the S nucleus is not consistent with the SEDs of typical Seyfert 2 nuclei, and in Lira et al. (2008) their T-ReCS N-band spectrum with a $1''.3$ slit shows evidence for star formation (e.g., PAH features). In our work, we showed that the circumnuclear star formation dominates the MIR flux at a $\sim 3''$ scale, and it is not surprising that the T-ReCS spectrum from the $1''.3$ slit shows PAH features because the T-ReCS flux and the IRS flux within the $3''.6$ aperture are almost the same (§3.3). We also showed that the X-ray-to-MIR luminosity ratio is consistent with typical AGNs if we consider only the AGN contribution at MIR after excluding contribution from the circumnuclear star-forming regions (§6.3).

Our deeper *Chandra* spectrum enabled us to better constrain the X-ray characteristics owing to improved statistics. On the basis of their first *Chandra* observation, Lira et al. (2002) presented spectral analysis of a composite X-ray spectrum of three hard sources including the S nucleus, and constrained the spectral shape of the S nucleus using X-ray hardness. We used two *Chandra* data sets totaling $\simeq 2.7$ times more effective exposure time, and were able to obtain spectra of the S nucleus alone. The relatively flat spectra we obtained are qualitatively consistent with the results by Lira et al. (2002). They assumed an absorbed power law model to constrain the allowed ranges of the photon index and absorption column density. Our spectral fits indicate that a single-component absorbed power law model gives an extremely flat photon index ($\Gamma < 0.25$), otherwise the quality of fit becomes significantly worse. The absence of a strong Fe-K fluorescent line in our spectrum strongly prefers the model consisting of two components, one of which is absorbed by Compton-thin matter ($N_H \sim 7 \times 10^{22}$ cm^{-2}), rather than a single absorbed power law.

The integrated spectrum of NGC 3256 measured with *XMM-Newton* provided a strong constraint on the flux of an Fe-K fluorescent line (Pereira-Santaella et al. 2011). Their upper limit on the flux is 3.5×10^{-15} erg cm^{-2} s^{-1} or 3.4×10^{-7} photons cm^{-2} s^{-1}. Our limit on the Fe-K flux (3.6×10^{-7} photons cm^{-2} s^{-1} for Model D) is almost the same as that obtained by Pereira-Santaella et al. (2011). We obtained spectra of the S nucleus alone, in contrast to the integrated spectra previously reported, and succeeded to set a limit on an Fe-K EW (< 190 eV for Model C and < 550 eV for Model D) that excludes the possibility of the presence of a Compton-thick AGN.

The AGN in the S nucleus is energetically much less important at MIR than the rest within NGC 3256 (§3.3.4), and previous estimates of the fractional AGN contribution within the galaxy seem not sensitive enough to detect the AGN. Alonso-Herrero et al. (2012) made SED modeling of the IRS spectrum extracted over a kpc-scale region to explore possible AGN contribution. They concluded that the AGN contributions to the whole-aperture MIR (at 6 and 24 μm) and IR luminosities are very small ($< 5\%$ and $< 1\%$, respectively). Our estimates of the AGN contribution to the S nucleus at $\sim 3''$ scale are $\sim 24\%$ and $\sim 2\%$ at 6 and 24 μm, respectively (§3.3.4). Since the entire-galaxy IRS spectrum of Alonso-Herrero et al. (2012) is about 8 times brighter than our nuclear ones (§2.1, 2.2), the AGN contributes to $\sim 3\%$ and $\sim 0.3\%$ of the whole-aperture MIR luminosities at 6 and 24 μm, respectively. Therefore, our results are consistent with those of Alonso-Herrero et al. (2012).

The absorption corrected X-ray luminosity of the S nucleus for the dual absorber model with Seyfert-like power-law continua (Model D), which we conclude most plausible, is 1.5×10^{40} erg s^{-1}. It is about 20% of the total X-ray luminosity integrated over NGC 3256, 7.4×10^{40} erg s^{-1}, measured with *XMM-Newton* (Pereira-Santaella et al. 2011).

7. SUMMARY AND CONCLUSIONS

NGC 3256 is the most luminous LIRG in the local universe ($z < 0.01$), and it is a merging galaxy with two (N and S) nuclei. Presence of an AGN in the S nucleus has been controversial. We examined spectrophotometric characteristics of the S nucleus at both near–mid-infrared (NIR–MIR) and X-ray using archival and published data, and found several pieces of evidence to support a low-luminosity AGN obscured by Compton-thin matter. The following are our findings and their implications.

We found in IRAC flux ratio maps that the S nucleus shows distinct photometric properties at 3.6–8.0 μm, most notably in its excess of 4.5 μm flux. In contrast, the N nucleus is similar in colors to the star-forming regions within the host galaxy. We applied the IRAC color-color diagrams for AGN diagnostics to the nuclear photometries for each nucleus, and found that the N and S nuclei show starburst- and AGN (power-law)-like SEDs, respectively. This difference originates from the 4.5 μm excess at the S nucleus.

Using high-resolution *HST* NICMOS images, we extracted a compact source at the S nucleus by subtracting the stellar component at 2.2 μm. The S nucleus consists of an unresolved (at 0$''$.26 FWHM) and a resolved (0$''$.75 FWHM or 128 pc after subtracting the instrumental resolution) component. The corresponding structures are not seen at 1.6 μm and shorter wavelengths. Because of its position and size, we identify its unresolved core with the compact MIR core (at 0$''$.30 FWHM resolution at 8.74 μm). The flux of the 2.2 μm core is consistent with our AGN spectral energy distribution (SED) model.

We analyzed the IRS nuclear spectrophotometries together with the IRAC nuclear photometries at 3.6–14.5 μm. The IRS spectrum of the S nucleus shows bluer colors at < 6 μm with respect to both the N nucleus and the IRS starburst template of Brandl et al. (2006) in a consistent way with the IRAC SED. We conducted SED modeling of the S nucleus to reproduce the high spatial-resolution (0$''$.36 aperture) T-ReCS N-band spectrophotometry (Díaz-Santos et al. 2010a) as well as the nuclear IRAC 4.5 μm and IRS data. Our AGN-starburst composite model (a heavily absorbed power-law AGN SED superposed on a mildly absorbed starburst-powered LIRG SED template) successfully reproduces both the deep silicate absorption at 9.7 μm within the 0$''$.36 aperture and the distinct PAH features with the 4–6 μm excess at $\sim 3''$ scale. We estimated A_V toward the AGN to be as large as 80 mag. All the MIR results point toward a heavily absorbed (but Compton-thin) type-2 AGN in the S nucleus. The AGN is most likely accompanied by circumnuclear star-forming regions.

We obtained a deep *Chandra* X-ray spectrum with $\simeq 2.7$ times more exposure time than in the previous study, and performed spectral analysis of a point-like source at the S nucleus. We found that a dual-component (for primary and scattered ones) power-law model successfully fits the hard spectrum. The inferred column density that is associated with the heavily absorbed primary component is $N_H = 7^{+19}_{-3} \times 10^{22}$ cm^{-2}, which is in the range typically observed in Seyfert 2s and is consistent with our MIR measurement. The lightly absorbed component can be interpreted as emission scattered by ionized medium in the opening part of the obscuring material around the AGN. The successful dual-component model suggests a Compton-thin type-2 AGN in the S nucleus. We also examined three other models for the S nucleus, namely a Compton-thick AGN, a single X-ray emitting compact source or a collection of such sources in the S nucleus, and thermal plasma with $kT < 1$ keV. We found that all of them are either rejected or less likely. A Compton-thick AGN is rejected because of a limit on EW of a fluorescent Fe-K emission line at 6.4 keV (< 190 eV for a reflection-dominated model). Models with compact stellar source(s) are less likely because of the observed high luminosity, hard spectrum, and/or small region size well within the *Chandra* resolution (0$''$.49 or 83 pc), although we cannot reject possibilities of models with multiple compact stellar sources. A model with the thermal plasma seems unusual, although it is statistically possible, because the low-kT plasma needs to be confined and hidden behind absorbing matter.

Our model with AGN is quantitatively consistent with most of the earlier studies that found no AGN in the S nucleus if we consider different aperture sizes and the star-forming circumnuclear region that dominates the MIR flux at $\sim 3''$ scale. In our best MIR SED model (the AGN-starburst composite model), the AGN contributes to $\sim 2\%$ and $\sim 0.2\%$ of the whole-aperture MIR luminosities at 6 and 24 μm, respectively. In our best X-ray model (a dual absorber model with Seyfert-like power-law continua), the absorption corrected X-ray luminosity of the S nucleus is about 20% of the total X-ray luminosity integrated over NGC 3256. In particular, we showed that the X-ray to MIR luminosity ratio of the AGN is consistent with that of typical Seyfert 2s if we exclude contribution of MIR flux from the circumnuclear star formation.

REFERENCES

Alexander, D. M., Bauer, F. E., Chapman, S. C., et al. 2005, ApJ, 632, 736
Alonso-Herrero, A., Quillen, A. C., Simpson, C., Efstathiou, A., & Ward, M. J. 2001, AJ, 121, 1369

Alonso-Herrero, A., Rieke, G. H., Rieke, M. J., & Scoville, N. Z. 2002, AJ, 124, 166

Alonso-Herrero, A., Rieke, G. H., Rieke, M. J., et al. 2006, ApJ, 650, 835

Alonso-Herrero, A., Colina, L., Packham, C., et al. 2006, ApJ, 652, L83

Alonso-Herrero, A., Pereira-Santaella, M., Rieke, G. H., & Rigopoulou, D. 2012, ApJ, 744, 2

Alonso-Herrero, A., Pereira-Santaella, M., Rieke, G. H., et al. 2013, ApJ, 765, 78

Anders, E., & Grevesse, N. 1989, Geochim. Cosmochim. Acta, 53, 197

Antonucci, R. 1993, ARA&A, 31, 473

Armus, L., Charmandaris, V., Bernard-Salas, J., et al. 2007, ApJ, 656, 148

Armus, L., Mazzarella, J. M., Evans, A. S., et al. 2009, PASP, 121, 559

Awaki, H., Koyama, K., Inoue, H., & Halpern, J. P. 1991, PASJ, 43, 195

Balucinska-Church, M., & McCammon, D. 1992, ApJ, 400, 699

Bauer, F. E., Brandt, W. N., Sambruna, R. M., et al. 2001, AJ, 122, 182

Bellocchi, E., Arribas, S., Colina, L., & Miralles-Caballero, D. 2013, A&A, 557, AA59

Bernard-Salas, J., Spoon, H. W. W., Charmandaris, V., et al. 2009, ApJS, 184, 230

Bohlin, R. C., Savage, B. D., & Drake, J. F. 1978, ApJ, 224, 132

Brandl, B. R., Bernard-Salas, J., Spoon, H. W. W., et al. 2006, ApJ, 653, 1129

Brauher, J. R., Dale, D. A., & Helou, G. 2008, ApJS, 178, 280

Cappi, M., Panessa, F., Bassani, L., et al. 2006, A&A, 446, 459

Caputi, K. I., Lagache, G., Yan, L., et al. 2007, ApJ, 660, 97

Cash, W. 1979, ApJ, 228, 939

Chiar, J. E., & Tielens, A. G. G. M. 2006, ApJ, 637, 774

Churchwell, E. 1990, A&A Rev., 2, 79

Churchwell, E. 2002, ARA&A, 40, 27

Comastri, A. 2004, in Supermassive Black Holes in the Distant Universe, ed. A. J. Barger (Dordrecht: Kluwer Academic Publishers), 245

da Cunha, E., Charmandaris, V., Díaz-Santos, T., et al. 2010, A&A, 523, AA78

Dadina, M. 2008, A&A, 485, 417

Dale, D. A., & Helou, G. 2002, ApJ, 576, 159

Desai, V., Armus, L., Spoon, H. W. W., et al. 2007, ApJ, 669, 810

Díaz-Santos, T., Alonso-Herrero, A., Colina, L., et al. 2010, ApJ, 711, 328

Díaz-Santos, T., Charmandaris, V., Armus, L., et al. 2010, ApJ, 723, 993

Díaz-Santos, T., Charmandaris, V., Armus, L., et al. 2011, ApJ, 741, 32

Done, C., Gierliński, M., & Kubota, A. 2007, A&A Rev., 15, 1

Donley, J. L., Koekemoer, A. M., Brusa, M., et al. 2012, ApJ, 748, 142

Doyon, R., Joseph, R. D., & Wright, G. S. 1994, ApJ, 421, 101

Emonts, B. H. C., Piqueras-López, J., Colina, L., et al. 2014, A&A, 572, AA40

Engelbracht, C. W., Rieke, G. H., Gordon, K. D., et al. 2008, ApJ, 678, 804

English, J., Norris, R. P., Freeman, K. C., & Booth, R. S. 2003, AJ, 125, 1134

Fazio, G. G., Hora, J. L., Allen, L. E., et al. 2004, ApJS, 154, 10

Fritz, T. K., Gillessen, S., Dodds-Eden, K., et al. 2011, ApJ, 737, 73

Fukazawa, Y., Hiragi, K., Mizuno, M., et al. 2011, ApJ, 727, 19

Gandhi, P., Horst, H., Smette, A., et al. 2009, A&A, 502, 457

George, I. M., Turner, T. J., Netzer, H., et al. 1998, ApJS, 114, 73

Genzel, R., Lutz, D., Sturm, E., et al. 1998, ApJ, 498, 579

Gilfanov, M., Grimm, H.-J., & Sunyaev, R. 2004, MNRAS, 347, L57

González-Martín, O., & Vaughan, S. 2012, A&A, 544, AA80

Graham, J. R., Wright, G. S., Meikle, W. P. S., Joseph, R. D., & Bode, M. F. 1984, Nature, 310, 213

Granato, G. L., Danese, L., & Franceschini, A. 1997, ApJ, 486, 147

Griffiths, R. E., Ptak, A., Feigelson, E. D., et al. 2000, Science, 290, 1325

Grimm, H.-J., Gilfanov, M., & Sunyaev, R. 2003, MNRAS, 339, 793

Guainazzi, M., Matt, G., & Perola, G. C. 2005, A&A, 444, 119

Hao, L., Weedman, D. W., Spoon, H. W. W., et al. 2007, ApJ, 655, L77

Ho, L. C., Feigelson, E. D., Townsley, L. K., et al. 2001, ApJ, 549, L51

Ho, L. C. 2008, ARA&A, 46, 475

Hopkins, P. F., Hernquist, L., Cox, T. J., et al. 2005, ApJ, 630, 705

Horst, H., Smette, A., Gandhi, P., & Duschl, W. J. 2006, A&A, 457, L17

Horst, H., Gandhi, P., Smette, A., & Duschl, W. J. 2008, A&A, 479, 389

Houck, J. R., Roellig, T. L., van Cleve, J., et al. 2004, ApJS, 154, 18

Hunt, L., Bianchi, S., & Maiolino, R. 2005, A&A, 434, 849

Iwasawa, K., Sanders, D. B., Teng, S. H., et al. 2011, A&A, 529, AA106

Ivezic, Z., & Elitzur, M. 1997, MNRAS, 287, 799

Kaaret, P., Schmitt, J., & Gorski, M. 2011, ApJ, 741, 10

Kalberla, P. M. W., Burton, W. B., Hartmann, D., et al. 2005, A&A, 440, 775

Kemper, F., Vriend, W. J., & Tielens, A. G. G. M. 2004, ApJ, 609, 826

Kim, D.-C., Sanders, D. B., Veilleux, S., Mazzarella, J. M., & Soifer, B. T. 1995, ApJS, 98, 129

Kotilainen, J. K., Moorwood, A. F. M., Ward, M. J., & Forbes, D. A. 1996, A&A, 305, 107

Lacy, M., Storrie-Lombardi, L. J., Sajina, A., et al. 2004, ApJS, 154, 166

Le Floc'h, E., Papovich, C., Dole, H., et al. 2005, ApJ, 632, 169

Leitherer, C., Schaerer, D., Goldader, J. D., et al. 1999, ApJS, 123, 3

Levenson, N. A., Sirocky, M. M., Hao, L., et al. 2007, ApJ, 654, L45

Lípari, S., Díaz, R., Taniguchi, Y., et al. 2000, AJ, 120, 645

Lira, P., Ward, M., Zezas, A., Alonso-Herrero, A., & Ueno, S. 2002, MNRAS, 330, 259

Lira, P., Gonzalez-Corvalan, V., Ward, M., & Hoyer, S. 2008, MNRAS, 384, 316

Magdziarz, P., & Zdziarski, A. A. 1995, MNRAS, 273, 837

Marshall, J. A., Herter, T. L., Armus, L., et al. 2007, ApJ, 670, 129

Markwardt, C. B. 2009, Astronomical Data Analysis Software and Systems XVIII, 411, 251

Martín-Hernández, N. L., Schaerer, D., Peeters, E., Tielens, A. G. G. M., & Sauvage, M. 2006, A&A, 455, 853

McClintock, J. E., & Remillard, R. A. 2006, in Compact Stellar X-ray Sources, ed. W. H. G. Lewin & M. van der Kils (Cambridge: Cambridge University Press), 157

Moran, E. C., Lehnert, M. D., & Helfand, D. J. 1999, ApJ, 526, 649

Mould, J. R., Huchra, J. P., Freedman, W. L., et al. 2000, ApJ, 529, 786

Nardini, E., Risaliti, G., Salvati, M., et al. 2008, MNRAS, 385, L130

Nardini, E., Risaliti, G., Watabe, Y., Salvati, M., & Sani, E. 2010, MNRAS, 405, 2505

Neff, S. G., Ulvestad, J. S., & Campion, S. D. 2003, ApJ, 599, 1043

Nenkova, M., Ivezić, Ž., & Elitzur, M. 2002, ApJ, 570, L9

Nenkova, M., Sirocky, M. M., Ivezić, Ž., & Elitzur, M. 2008, ApJ, 685, 147

Nenkova, M., Sirocky, M. M., Nikutta, R., Ivezić, Ž., & Elitzur, M. 2008, ApJ, 685, 160

Noguchi, K., Terashima, Y., Ishino, Y., et al. 2010, ApJ, 711, 144

Norris, R. P., & Forbes, D. A. 1995, ApJ, 446, 594

Pereira-Santaella, M., Alonso-Herrero, A., Rieke, G. H., et al. 2010, ApJS, 188, 447

Pereira-Santaella, M., Alonso-Herrero, A., Santos-Lleo, M., et al. 2011, A&A, 535, AA93

Petric, A. O., Armus, L., Howell, J., et al. 2011, ApJ, 730, 28

Polletta, M., Tajer, M., Maraschi, L., et al. 2007, ApJ, 663, 81

Ptak, A., Serlemitsos, P., Yaqoob, T., & Mushotzky, R. 1999, ApJS, 120, 179

Ranalli, P., Comastri, A., & Setti, G. 2003, A&A, 399, 39

Rich, J. A., Torrey, P., Kewley, L. J., Dopita, M. A., & Rupke, D. S. N. 2012, ApJ, 753, 5

Rieke, G. H., Young, E. T., Engelbracht, C. W., et al. 2004, ApJS, 154, 25

Ruiz, A., Miniutti, G., Panessa, F., & Carrera, F. J. 2010, A&A, 515, AA99

Sajina, A., Lacy, M., & Scott, D. 2005, ApJ, 621, 256

Sakamoto, K., Ho, P. T. P., & Peck, A. B. 2006, ApJ, 644, 862

Sakamoto, K., Aalto, S., Combes, F., Evans, A., & Peck, A. 2014, ApJ, 797, 90

Sanders, D. B., & Mirabel, I. F. 1996, ARA&A, 34, 749

Sanders, D. B., Mazzarella, J. M., Kim, D.-C., Surace, J. A., & Soifer, B. T. 2003, AJ, 126, 1607

Sawicki, M. 2002, AJ, 124, 3050

Shu, X. W., Yaqoob, T., & Wang, J. X. 2011, ApJ, 738, 147

Siebenmorgen, R., Krügel, E., & Spoon, H. W. W. 2004, A&A, 414, 123

Siebenmorgen, R., Haas, M., Pantin, E., et al. 2008, A&A, 488, 83

Sirocky, M. M., Levenson, N. A., Elitzur, M., Spoon, H. W. W., & Armus, L. 2008, ApJ, 678, 729

Silva, L., Granato, G. L., Bressan, A., & Danese, L. 1998, ApJ, 509, 103

Smith, R. K., Brickhouse, N. S., Liedahl, D. A., & Raymond, J. C. 2001, ApJ, 556, L91

Smith, J. D. T., Armus, L., Dale, D. A., et al. 2007, PASP, 119, 1133

Smith, J. D. T., Draine, B. T., Dale, D. A., et al. 2007, ApJ, 656, 770

Snyder, G. F., Hayward, C. C., Sajina, A., et al. 2013, ApJ, 768, 168

Spoon, H. W. W., Marshall, J. A., Houck, J. R., et al. 2007, ApJ, 654, L49

Stern, D., Eisenhardt, P., Gorjian, V., et al. 2005, ApJ, 631, 163

Stierwalt, S., Armus, L., Surace, J. A., et al. 2013, ApJS, 206, 1

Storchi-Bergmann, T., Kinney, A. L., & Challis, P. 1995, ApJS, 98, 103

Strickland, D. K., Heckman, T. M., Weaver, K. A., & Dahlem, M. 2000, AJ, 120, 2965

Strickland, D. K., Heckman, T. M., Colbert, E. J. M., Hoopes, C. G., & Weaver, K. A. 2004, ApJS, 151, 193

Strickland, D. K., Heckman, T. M., Colbert, E. J. M., Hoopes, C. G., & Weaver, K. A. 2004, ApJS, 151, 193

Sturm, E., Lutz, D., Verma, A., et al. 2002, A&A, 393, 821

Surace, J. A., Shupe, D. L., & Fang, F. 2004, VizieR Online Data Catalog, 2255, 0

Terashima, Y., Iyomoto, N., Ho, L. C., & Ptak, A. F. 2002, ApJS, 139, 1

Terashima, Y., & Wilson, A. S. 2003, ApJ, 583, 145

Thuan, T. X., Bauer, F. E., & Izotov, Y. I. 2014, MNRAS, 441, 1841

Tsujimoto, M., Hosokawa, T., Feigelson, E. D., Getman, K. V., & Broos, P. S. 2006, ApJ, 653, 409

Tüllmann, R., Pietsch, W., Rossa, J., Breitschwerdt, D., & Dettmar, R.-J. 2006, A&A, 448, 43

Turner, T. J., George, I. M., Nandra, K., & Mushotzky, R. F. 1997, ApJS, 113, 23

Vasudevan, R. V., & Fabian, A. C. 2007, MNRAS, 381, 1235

Vasudevan, R. V., & Fabian, A. C. 2009, MNRAS, 392, 1124

Veilleux, S., Kim, D.-C., Sanders, D. B., Mazzarella, J. M., & Soifer, B. T. 1995, ApJS, 98, 171

Verley, S., Hunt, L. K., Corbelli, E., & Giovanardi, C. 2007, A&A, 476, 1161

Wood, D. O. S., & Churchwell, E. 1989, ApJS, 69, 831

Yan, M., Sadeghpour, H. R., & Dalgarno, A. 1998, ApJ, 496, 1044

Zepf, S. E., Ashman, K. M., English, J., Freeman, K. C., & Sharples, R. M. 1999, AJ, 118, 752

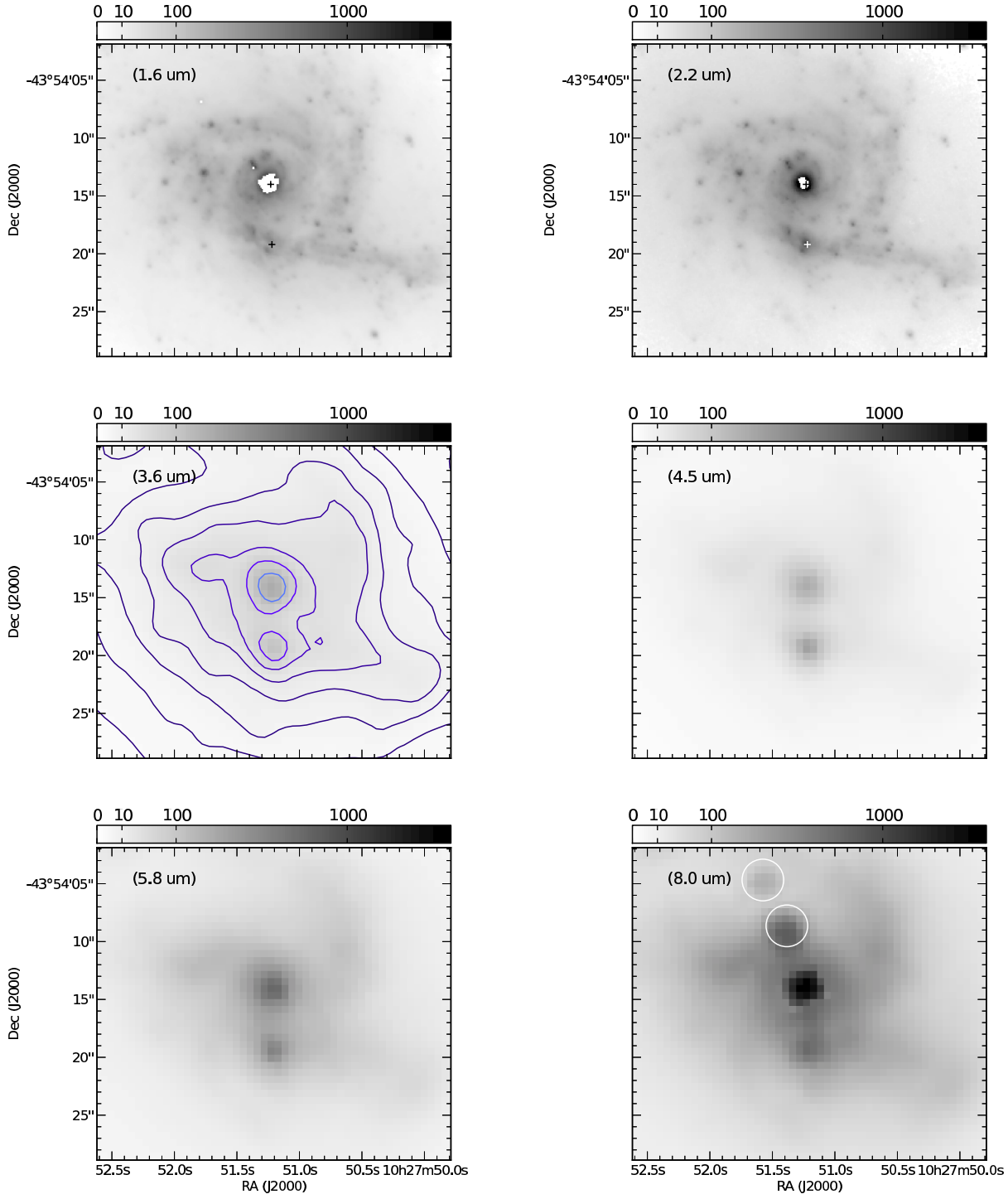Zhu, Y.-N., Wu, H., Cao, C., & Li, H.-N. 2008, ApJ, 686, 155

Figure 1. *HST* NICMOS F160W and F222M images (upper row) and *Spitzer* IRAC four channel images (middle and lower rows) of NGC 3256 around the N and S nuclei. North is up and east is to the left. Both NICMOS and IRAC images are shown in a square root scale as indicated in scale bars (in units of MJy/steradian) for each panel. The N nucleus is saturated in the two NICMOS images, and are masked. Positions of the two nuclei in radio continuum (Neff et al. 2003) are marked with crosses on the NICMOS images. Contours at logarithmic steps are overlaid on the IRAC 3.6 μm image. In the lower right panel (IRAC 8.0 μm), two white circles indicate locations of artifacts (known as the "bandwidth effect"; IRAC instrument handbook) caused by the saturated N nucleus. Also in this panel, the saturated pixels around the N nucleus are fixed as described in the main text.
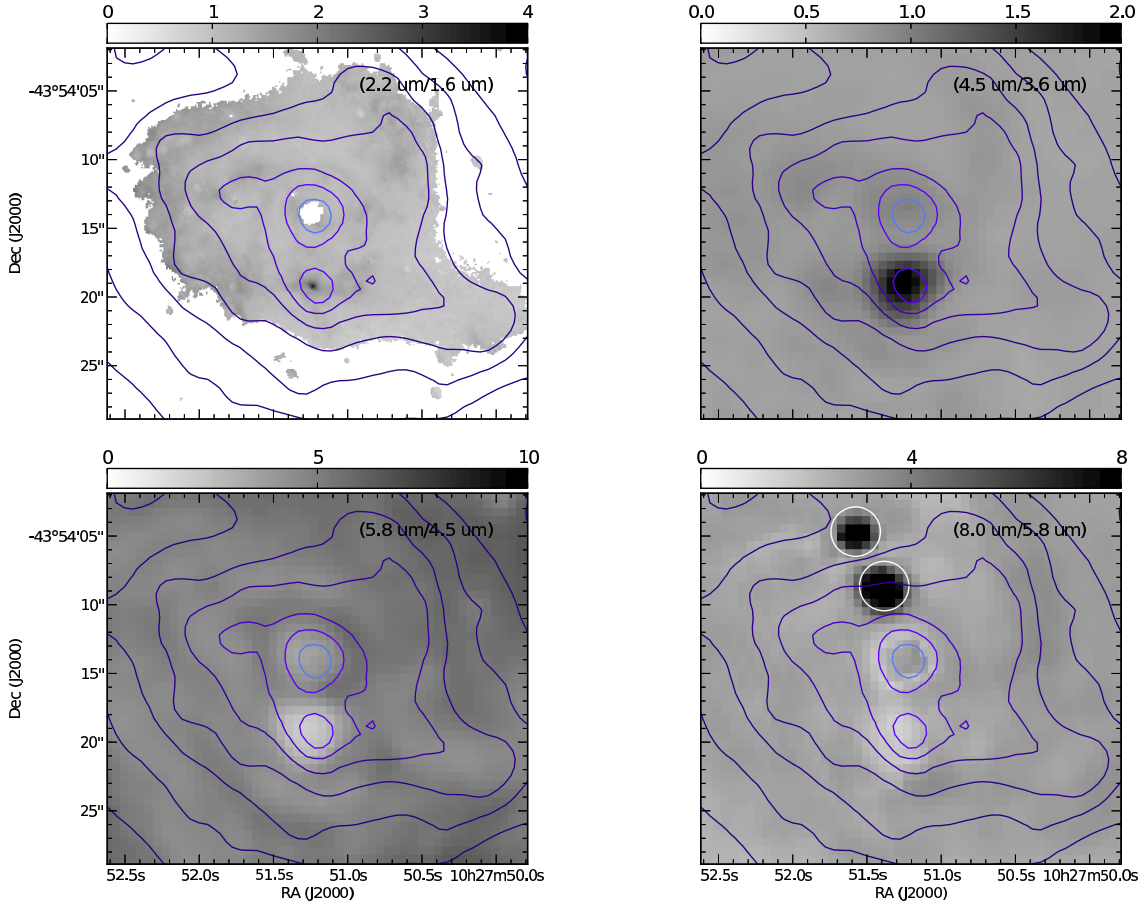
Figure 2. Flux ratio maps of NICMOS F222M/F160W (upper left), IRAC 4.5 μm/3.6 μm (upper right), 5.8 μm/4.5 μm (lower left), and 8.0 μm/5.8 μm (lower right) around the N and S nuclei. All images are shown in the same sky area as in Figure 1. Contours of the IRAC 3.6 μm image shown in Figure 1 are overlaid on all flux ratio maps for positional references. Flux ratio scales are indicated in scale bars for each panel. Outer fainter regions with signal-to-noise ratio being less than 3.0 per pixel are masked in the F222M/F160W image. Two white circles in the 8.0 μm/5.8 μm map (lower right) indicate areas that are affected by the artifacts in the 8.0 μm image as shown in Figure 1.
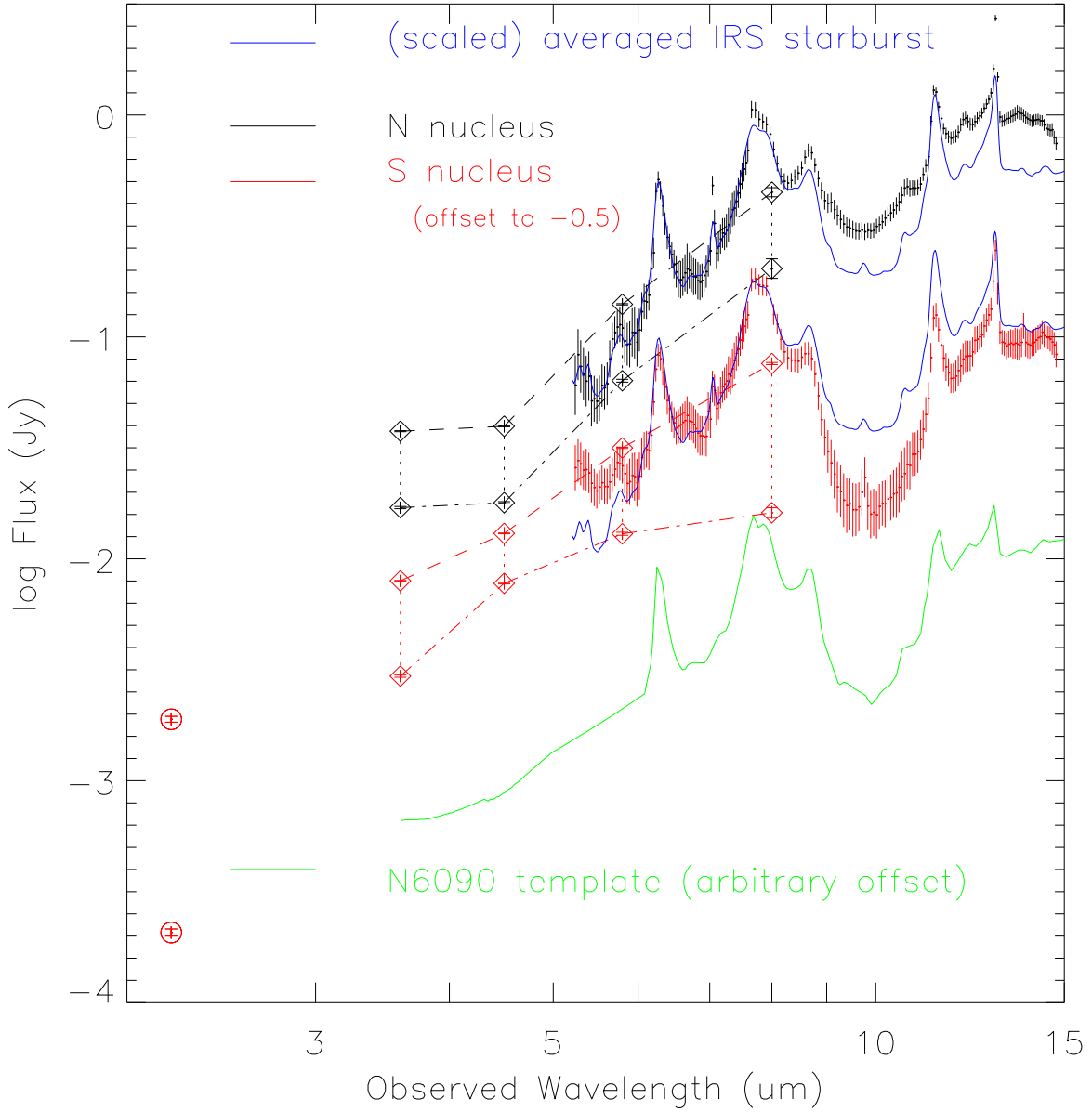
Figure 3. The IRS spectra and IRAC photometries of the N (black; top) and S (red; middle) nuclei, and the NICMOS photometry of the S nucleus (red). All photometries for the S nucleus are shown with an offset of −0.5 for clarity of the figure. IRAC fluxes of each nucleus are shown both for nuclear fluxes (diamonds connected by dot-dashed lines) and adjusted fluxes (to match the IRS spectra; diamonds connected by dashed lines). See the main text for the details of the adjustment. We also show the NICMOS F222M nuclear photometry of an unresolved compact source (lower) and sum of the unresolved and resolved sources (upper) at the S nucleus with red circles. The error bars are for ±1σ. Each blue solid line shows the starburst IRS spectrum of Brandl et al. (2006) that is redshifted to NGC 3256 and scaled at 6.0–8.0 μm for each nucleus. The LIRG SED template of NGC 6090 arbitrary scaled for clarify of the figure is also shown with green solid line (bottom).
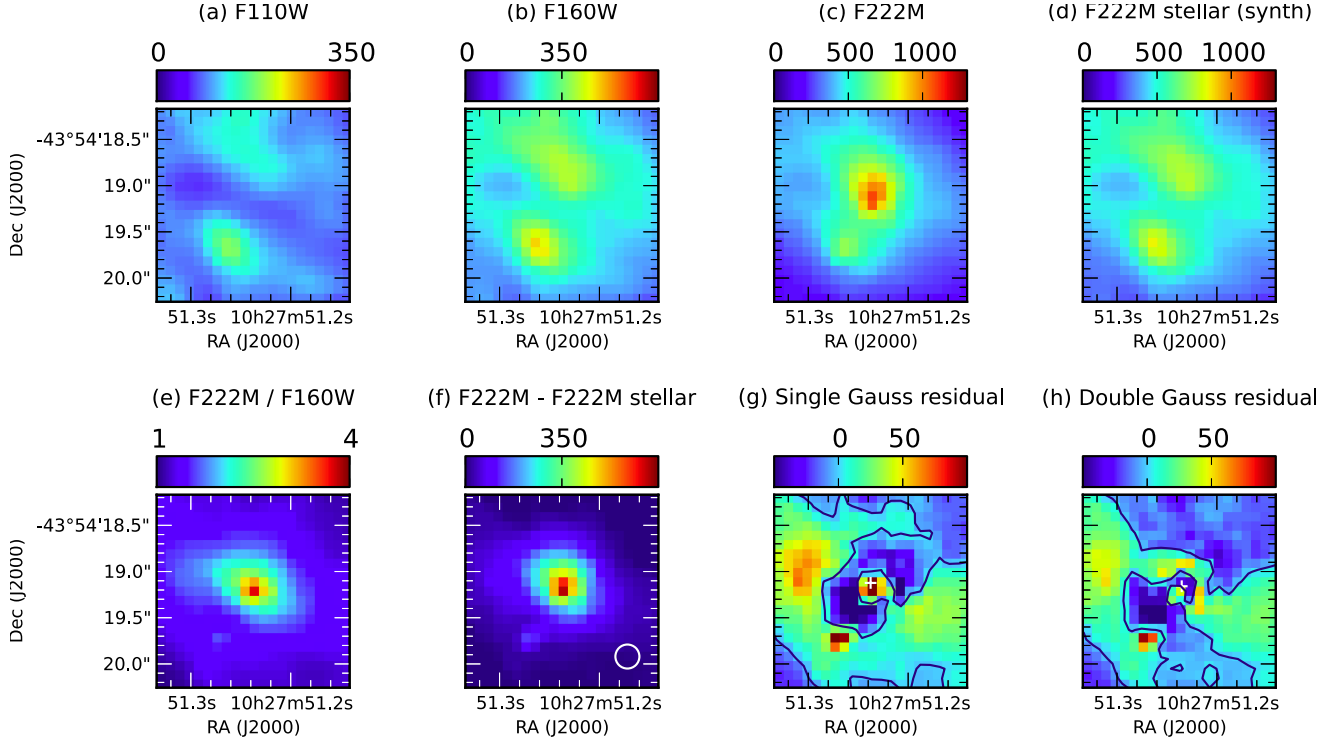
Figure 4. Zoom-up NICMOS images of the S nucleus and results of our analysis. (a)–(c) NICMOS F110W, F160W, and F222M images. (d) Synthetic F222M image of the stellar component. See the main text for the details of the synthesis. (e) A flux ratio image of F222M/F160W. (f) The F222M nuclear component, made by subtracting the synthetic F222M stellar component image from the observed F222M image. The NICMOS resolution (0.″26 FWHM) is indicated by a white circle. (g)–(h) The residual images of the F222M nuclear component after subtracting the fitted Gaussian models. The panel (g) shows a case of single-Gaussian model, and (h) shows a case of double-Gaussian model. The fitted positions of Gaussian components are marked with white pluses in panels (g) and (h). All panels are shown in linear scale, and flux (in units of MJy/steradian) and flux ratio (for only panel f) scale are indicated in scale bars for each panel. The zero flux levels in the residual images are also indicated by black contours.
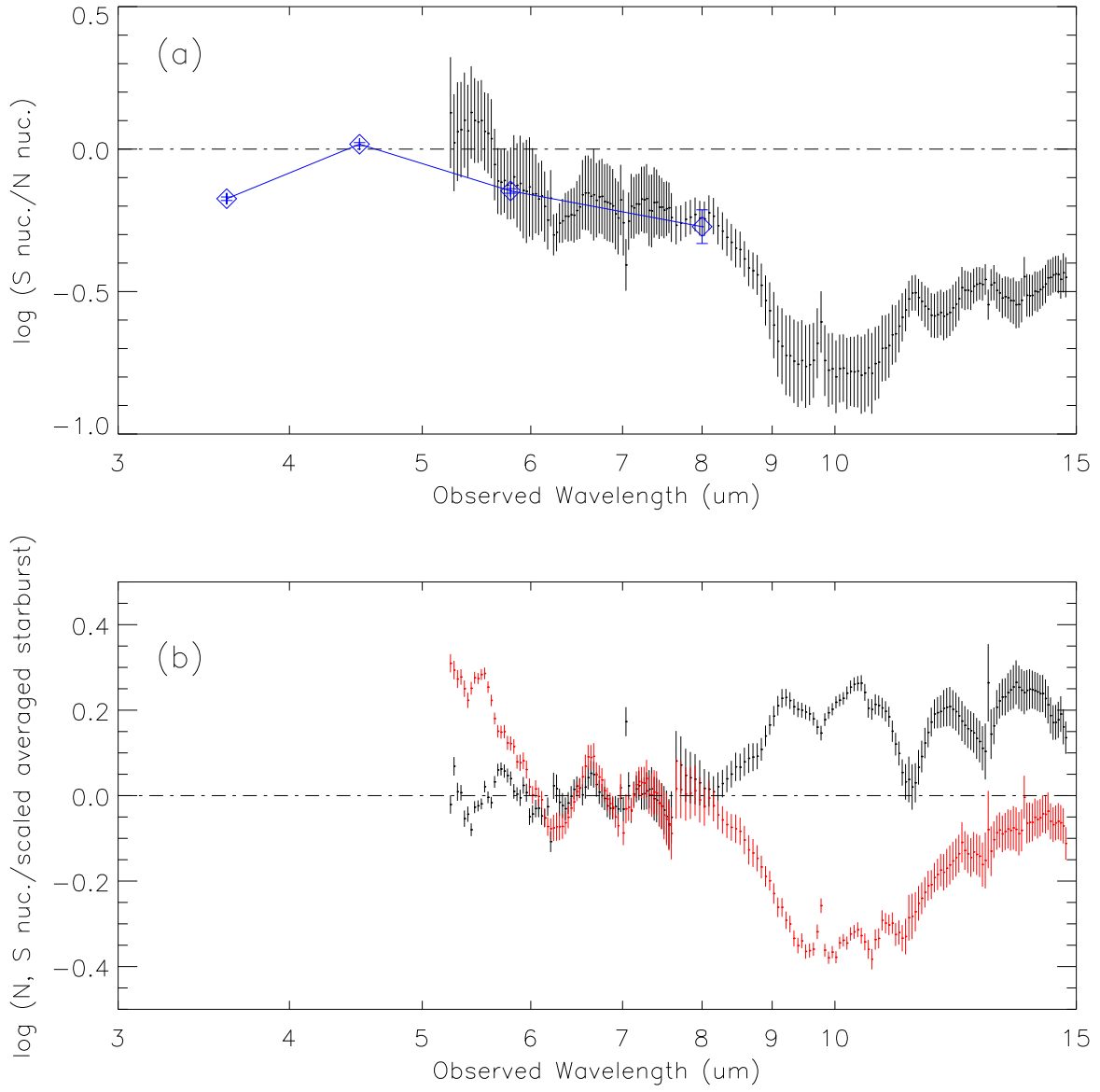
Figure 5. (a) The spectrum of the flux ratio between the N and S nuclei. The IRS data are in black and the IRAC data are in blue. (b) The spectra of the flux ratio between the individual nuclei and the IRS starburst template of Brandl et al. (2006). The latter is redshifted and scaled at 6.0–8.0 μm for each nucleus. The N nucleus is shown in black and the S nucleus is in red. Error bars are $\pm 1\sigma$.
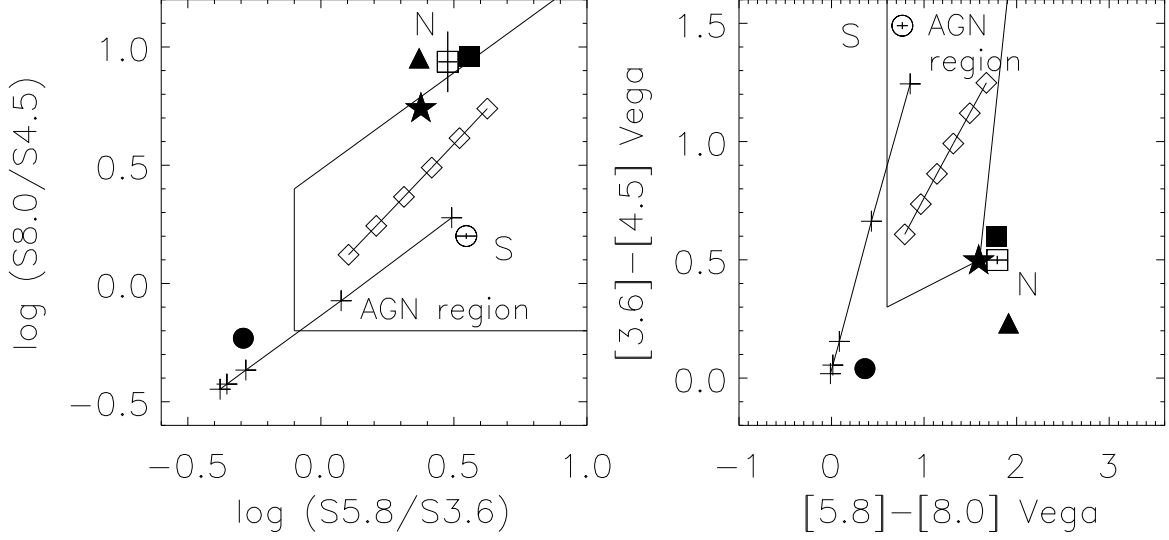
Figure 6. The IRAC color-color diagrams of the N (open square) and S (open circle) nuclei with boundaries for AGN selection. Error bars are $\pm 1\sigma$. Also shown in filled symbols are rest frame colors/flux ratios of ULIRG IRAS 22491-1808 from Polletta et al. (2007) (square), starburst M 82 from Polletta et al. (2007) (star), a template of normal star-forming spiral galaxy from Dale & Helou (2002) (triangle), and a representative elliptical galaxy from Polletta et al. (2007) (circle). Connected diamonds are for pure power-law SEDs, and each triangle corresponds to a power-law index of α from -0.5 (lower left) to -3.0 (upper right) in steps of 0.5. Connected pluses represent colors/flux ratios for pure blackbody SEDs, and each plus corresponds to a blackbody temperature of 600 K (upper right), 1000 K, 3000 K, 6000 K, and 10000 K (lower left). The boundaries for AGN selection are from Donley et al. (2012).
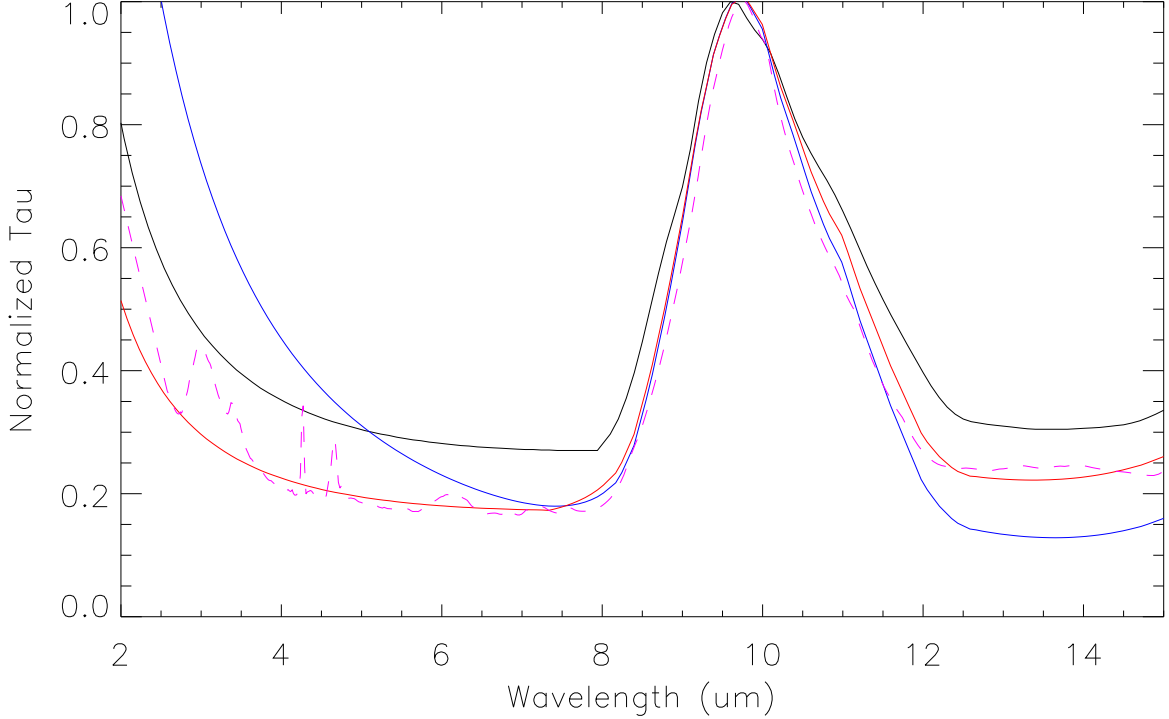

Figure 7. Comparison of extinction curves used in our SED modeling. We show the extinction curve of Chiar & Tielens (2006) for the Galactic center (black solid line), the original PAHFIT (Smith et al. 2007b) extinction curve (blue solid line), the original extinction curve of Fritz et al. (2011) (broken magenta line), and the modified PAHFIT extinction curve (red solid line) to reproduce the curve of Fritz et al. (2011). See the main text for the details of the modified PAHFIT extinction curve.
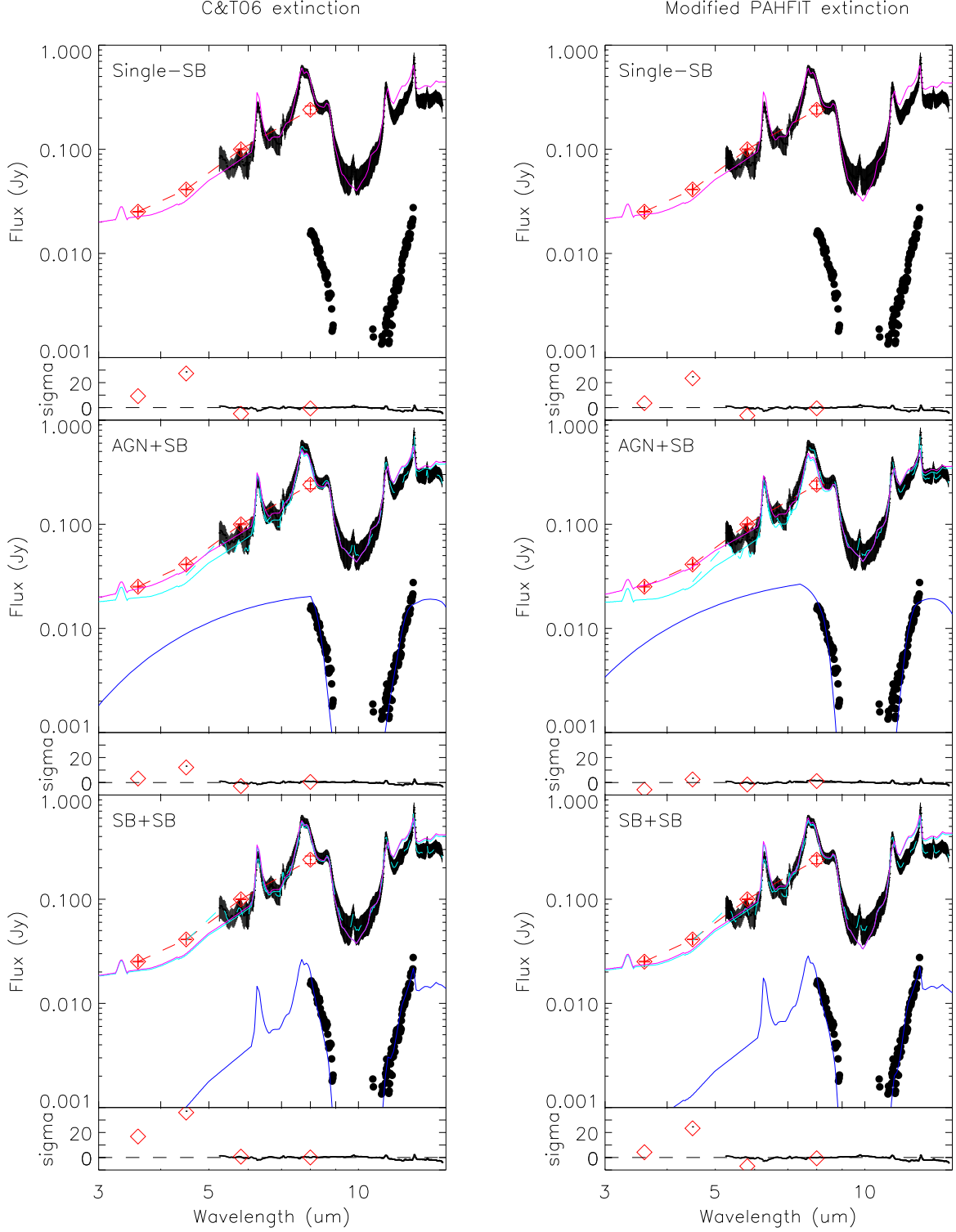
Figure 8. SED modeling results for the S nucleus. The absorbed single-starburst model (Single-SB), the AGN-starburst composite model (AGN+SB), and the starburst-starburst composite model (SB+SB) are shown in the top, middle, and bottom rows, respectively. Results with the extinction curve of Chiar & Tielens (2006) and the modified PAHFIT extinction curve are shown in the left and right columns, respectively. The adjusted IRAC photometries as shown in Figure 3 (connected red diamonds with $\pm 1\sigma$ error bars), the IRS (with $\pm 1\sigma$ error bars; black) and T-ReCS spectrophotometries (black) are shown in all panels. For the absorbed single-starburst model, we overlay the best-fit models with magenta solid lines. For both the AGN-starburst and starburst-starburst composite models, we overlay the best fit models for the T-ReCS (blue), residual 4.5 μm–IRS spectrophotometries (observed−best-fit T-ReCS model) (cyan), and sum of the two components (magenta). The sigma ((observation−model)/observation noise) spectra of the IRS spectrophotometries (black) and synthetic IRAC fluxes from the best-fit models (red diamonds) are shown for each panel.
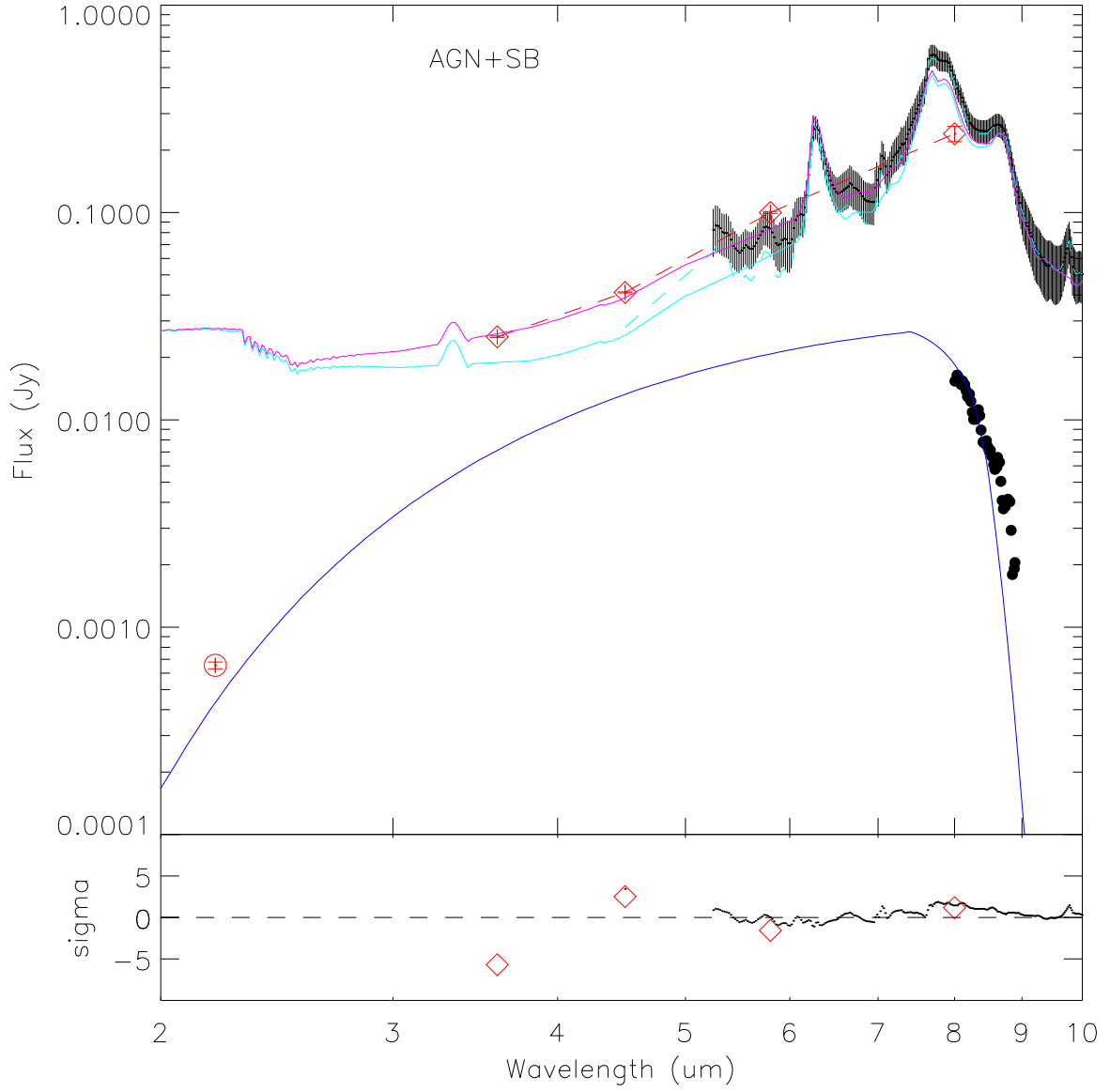
Modified PAHFIT extinction

Figure 9. The best SED modeling result for the S nucleus with the AGN-starburst composite model and the modified PAHFIT extinction curve at 2.0–10 μm. The same colors and symbols of Figure 8 are used. The NICMOS photometry at 2.2 μm of the unresolved core is also shown with a $\pm 1\sigma$ error bar (red circle).
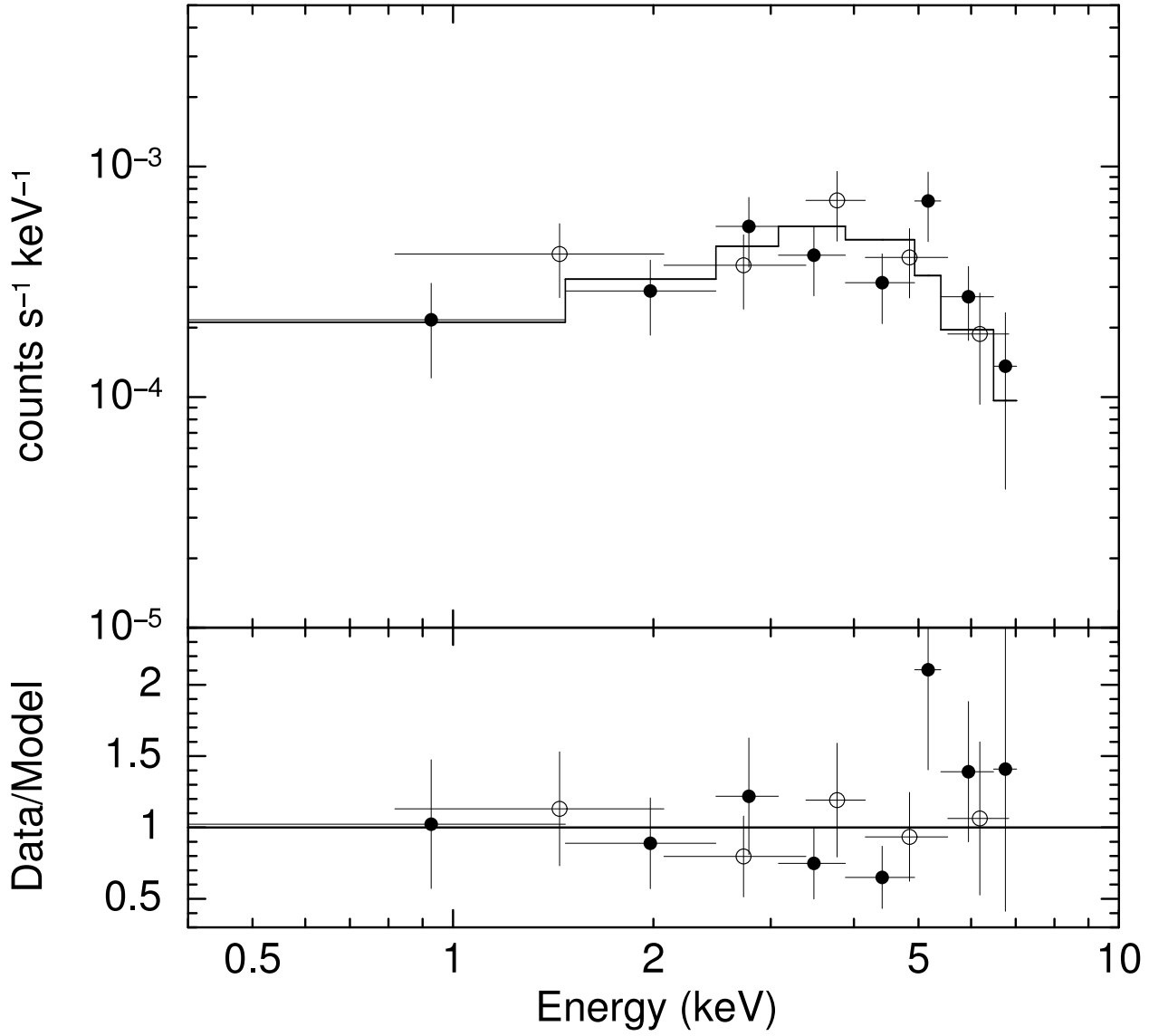
Figure 10. Observed *Chandra* spectra of the S nucleus for the first (open circles) and second (filled circles) observations. Data are binned for presentation purpose. (Upper panel) Observed spectra and the best-fit model (Model D, solid line). Only the model for the second observation is shown for clarity. (Lower panel) Data/Model ratio.

The error bars are for $\pm 1\sigma$.
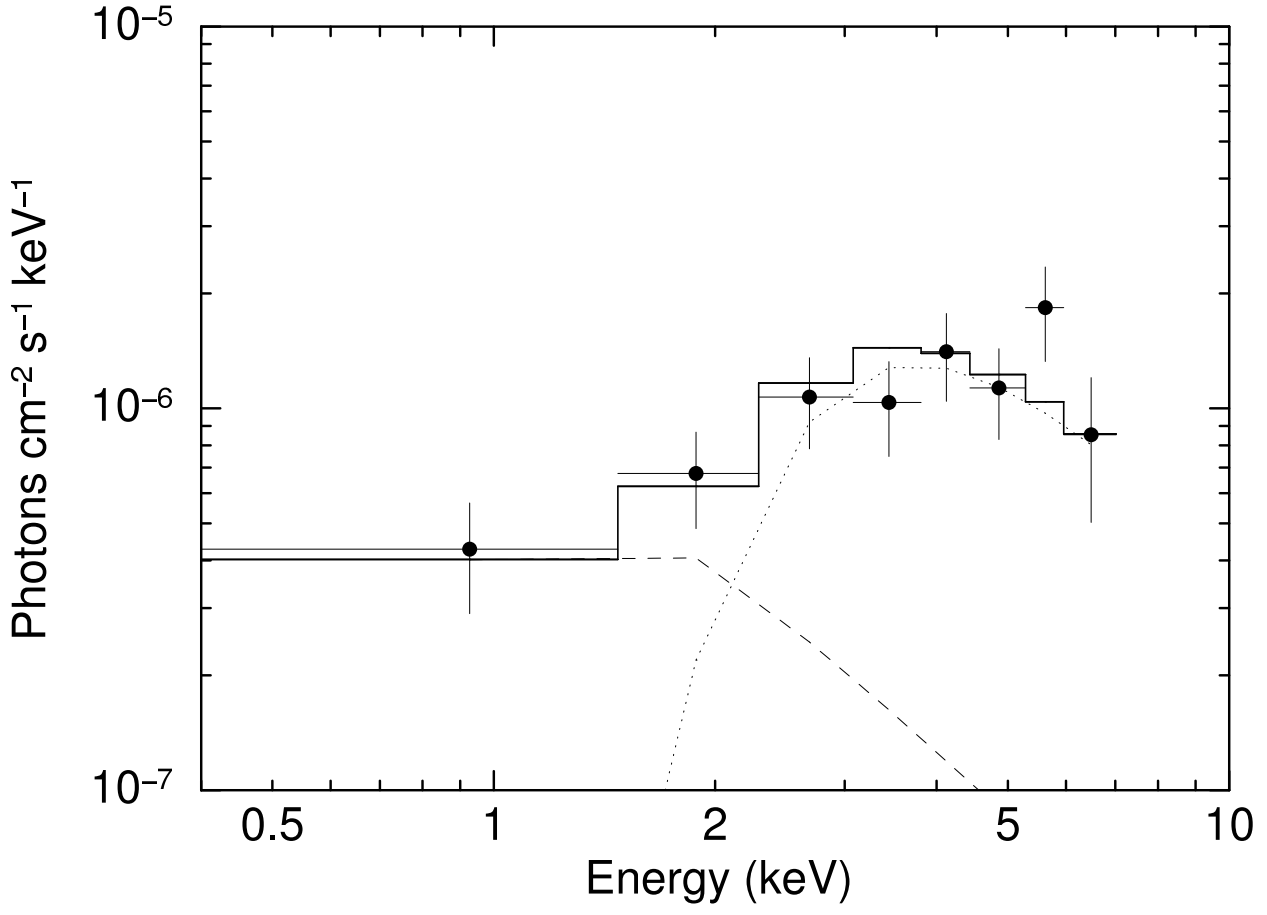
Figure 11. Unfolded *Chandra* spectrum of the S nucleus. The responses of detector and telescope are unfolded. The spectra from the two observations are combined for presentation purpose. The error bars are for $\pm 1\sigma$. The best-fit model (Model D, solid line), lightly (dashed line), and heavily (dotted line) absorbed components are shown for comparison.

Table 1
IRAC photometry results.

| Channel	Flux (mJy)[a]	
	N nucleus	S nucleus
Nuclear photometry[b]		
3.6 μm	17.0 ± 0.2	9.4 ± 0.1
4.5 μm	17.9 ± 0.2	24.5 ± 0.2
5.8 μm	63.5 ± 0.9	41.0 ± 0.6
8.0 μm	203 ± 22[c]	51.0 ± 2.7
Adjusted for the IRS spectra[d]		
3.6 μm	34.7 ± 0.4	25.2 ± 0.2
4.5 μm	36.6 ± 0.4	41.2 ± 0.3
5.8 μm	130 ± 1.9	100 ± 1.1
8.0 μm	415 ± 44[c]	240 ± 20

[a]Uncertainties are for $\pm 1\sigma$.
[b]Photometry with 2$\farcs$8 diameter aperture with aperture correction.
[c]The photometry is made on the image corrected for the saturation at the N nucleus. See the main text for the details.
[d]IRAC fluxes adjusted for the same level of circumnuclear flux contamination for the IRS resolution. See the main text for the details of the adjustment.

Table 2
Results of the double-Gaussian model fitting to the S nucleus on the stellar-component subtracted F222M image.

	compact source	extended source
Position	(J2000)	
RA	10:27:51.24[a]	
DEC	-43:54:19.2[a]	
source size	(FWHM in arcsec)	
	unresolved[b]	$0\farcs75 \pm 0\farcs01$ [c]
Flux	(mJy)[d]	
	0.65 ± 0.02	5.33 ± 0.16

[a]Uncertainties (0$\farcs$2) are dominated by global astrometry solution. See the main text for the details.
[b]Assumed to be unresolved at 0$\farcs$26 FWHM.
[c]After correcting for the instrumental resolution of 0$\farcs$26 FWHM.
[d]Uncertainties are for $\pm 1\sigma$.

Table 3
MIR spectrophotometry model fitting results.

Extinction curve	Data to fit	models[a]	Single-SB[b]	AGN+SB		SB+SB	
				0$\farcs$36 aperture	$\simeq 3''$ aperture	0$\farcs$36 aperture	$\simeq 3''$ aperture
Chiar & Tielens (2006)[c]	4.5 μm+IRS+T-ReCS	$\tau_{9.7}$	1.04 ± 0.01	9.4 ± 0.4	0.68 ± 0.01	6.8 ± 0.3	0.98 ± 0.02
		reduced χ^2	4.09	1.4	1.4	1.2	4.4
	IRS+T-ReCS	reduced χ^2	0.90	1.4	0.77	1.2	0.87
Original PAHFIT	4.5 μm+IRS+T-ReCS	$\tau_{9.7}$	0.00	8.0 ± 0.4	0.0	6.0 ± 0.3	0.0
		reduced χ^2	5.80	3.6	5.2	2.7	6.0
	IRS+T-ReCS	reduced χ^2	1.09	3.6	1.08	2.7	1.11
Modified PAHFIT[d]	4.5 μm+IRS+T-ReCS	$\tau_{9.7}$	1.21 ± 0.05	12.7 ± 0.5	0.48 ± 0.04	8.3 ± 0.4	1.10 ± 0.02
		reduced χ^2	3.58	1.2	0.79	1.2	3.5
	IRS+T-ReCS	reduced χ^2	0.90	1.2	0.74	1.2	0.86

[a]Models: Single-SB = absorbed single-starburst model; AGN+SB = AGN-starburst composite model; SB+SB = starburst-starburst composite model.
[b]T-ReCS data are not used for this model.
[c]Toward Galactic center.
[d]Modified to reproduce the extinction curve of Fritz et al. (2011). See the main text for the details.

Table 4
Chandra Observation Log.

Observation ID[a]	Date[b]	Exposure[c] (ksec)	Counts[d]
835	2000 Jan 5	16.2	39
3569	2003 May 23	27.2	62

[a]Observation identification number.
[b]Observation start date.
[c]Exposure time after data screening.
[d]Number of counts after background subtraction in 0.5-7 keV.

Table 5
Results of X-ray spectral fits with power law model.

Model[a]	$N_{H,1}$ $(10^{22}$ cm$^{-2})$	$N_{H,2}$ $(10^{22}$ cm$^{-2})$	f	Photon index	Norm.	Constant	C/dof	EW (eV)	$F_{2-10\ \mathrm{keV}}$	$L_{2-10\ \mathrm{keV}}$
(1)	(2)	(3)	(4)	(5)	(6)	(7)	(8)	(9)	(10)	(11)
A	0.054 (<0.97)	...	...	$-0.42^{+0.67}_{-0.39}$	0.067	$0.94^{+0.40}_{-0.27}$	76.8/90	<150	11.5	1.7
B	3.6	...	...	1.8^a	2.15	0.92	94.5/91^b	...	...	...
C	0 (< 0.27)	...	...	1.8^a	46.4	$0.93^{+0.39}_{-0.27}$	78.1/91	<190	9.26	1.4
D	$0.34^{+1.56}_{-0.25}$	7^{+19}_{-3}	$0.943^{+0.037}_{-0.149}$	1.8^a	2.93	$0.95^{+0.40}_{-0.27}$	78.6/89	< 550	6.33	1.5

Note. — (1) Spectral models. The Galactic absorption ($N_H = 9.14 \times 10^{20}$ cm^{-2}) is applied to all the models. (2), (3) Intrinsic absorption column density. (4) The fraction of continuum absorbed by a large column density ($N_{H,2}$). (5) Photon index of power law component. (6) Normalization of power law in units of 10^{-5} photons cm^{-2} s^{-1} at 1 keV. (7) Constant factor relative to the first observation. (8) C statistic and degrees of freedom. (9) Upper limit on the equivalent width of fluorescent Fe-Kα line in units of eV. (10) Observed flux in the 2–10 keV band for the first observation in units of 10^{-14} erg s^{-1} cm^{-2}. (11) Luminosity corrected for absorption in the 2–10 keV band for the first observation in units of 10^{40} erg s^{-1}.
^{a} Fixed parameter.
^{b} Errors, limit on Fe-K line equivalent width, flux, and luminosity are not shown for this model since the value of C statistic is significantly worse than those for other models.

Table 6
Results of X-ray spectral fits with thermal model.

Model[a]	N_H $(10^{22}$ cm$^{-2})$	N_H $(10^{22}$ cm$^{-2})$	kT	Norm.	kT	Norm.	Constant	C/dof	$F_{2-10\ \mathrm{keV}}$	$L_{2-10\ \mathrm{keV}}$
(1)	(2)	(3)	(4)	(5)	(6)	(7)	(8)	(9)	(10)	(11)
E	$5.1^{+3.3}_{-1.9}$	...	64^a (>9.4)	6.71	64^a (>1.2)	0.428	$0.93^{+0.39}_{-0.26}$	77.6/88	6.98	1.4
F	$4.3^{+4.0}_{-2.0}$	$1.3^{+1.0}_{-0.5}$	64^a (>9.7)	7.44	1.0^b	0.798	$0.95^{+0.40}_{-0.28}$	77.3/88	7.06	1.4

Note. — (1) Spectral models. The Galactic absorption ($N_H = 9.14 \times 10^{20}$ cm^{-2}) is applied to all the models. (2) Intrinsic absorption column density for heavily absorbed APEC component. (3) Intrinsic absorption column density common to both APEC components. (4) Temperature of heavily absorbed APEC component. (5) Normalization of heavily absorbed APEC component in units of $10^{-19}/(4\pi(D_A(1+z))^2/\int n_e n_H dV$, where D_A is the angular size distance to the source (cm), n_e is the electron density (cm^{-3}), and n_H is the hydrogen density (cm^{-3}). (6) Temperature of lightly absorbed APEC component. (7) Normalization of lightly absorbed APEC component in units of $10^{-19}/(4\pi(D_A(1+z))^2/\int n_e n_H dV$. (8) Constant factor. (9) C statistic and degrees of freedom. (10) Observed flux in the 2–10 keV band for the first observation in units of 10^{-14} erg s^{-1} cm^{-2}. (11) Luminosity corrected for absorption in the 2–10 keV band for the first observation in units of 10^{40} erg s^{-1}.
^{a} Pegged at the highest temperature allowed in the fit.
^{b} Fixed parameter.